nature electronics

Supplementary information https://doi.org/10.1038/s41928-024-01271-4

A wearable echomyography system based on a single transducer

In the format provided by the authors and unedited

Table of contents

Supplementary Table 3 | Comparison with other fully integrated wearable ultrasound devices.

Supplementary Table 4 | Comparison among different EcMG studies for hand gesture recognition.

Supplementary Table 5 | Accuracies of hand gesture recognition based on EMG and EcMG.

Caption for Supplementary Video 1

Caption for Supplementary Video 2

Caption for Supplementary Video 3

References

Supplementary Note 1 | Existing wearable devices for noninvasive sensing of the human body

Many wearable electronic devices have been reported in the past decade for sensing physiological signals from the human body. These devices usually have small form factors and soft encapsulation layers to minimize restrictions to body motions. They could sense a wide range of signals from the human body, such as temperature[1], body motion[2], skin curvature[3], contact pressure with surrounding environment[4,5], biochemical components in sweat and interstitial fluids[6,7], and peripheral capillary oxygen saturation[1]. Wearable devices are based on different sensing mechanisms to acquire multimodal parameters, as elaborated in the following.

- Local field potential sensors

Local field potential sensors, such as electromyogram (EMG), use electrodes to collect biopotentials on the skin surface generated by motor units. EMG sensors are widely applied for different applications, such as forearm muscles for hand gesture recognition[8], hind limb muscles for monitoring spinal cord injury[9], respiration muscles for diagnosing breathing functions[10], and facial muscles for managing oropharyngeal swallowing disorder[11], nonverbal expression[12], and oral cancers[13].

- Inertial Measurement Unit (IMU) sensors

IMU sensors commonly contain at least three-axis accelerometers, which can detect body motion and skin surface vibrations in 3D space. Advanced IMU sensors also integrate three-axis gyroscopes that measure angular rate and three-axis magnetometers that measure magnetic field surrounding the system. IMU sensors can be attached to different body positions, like chest, neck, arm, and hand. Analyzing the data of IMU sensors can extract the heart rate[1], respiration rate[1], speech[14], pruritus[15], and body orientation[2].

- Strain and pressure sensors

Strain and pressure sensors are usually composed of resistive materials or capacitive structures that respond to deformation or pressure. They are widely used for the detection of skin surface motion and force to monitor arterial pulsation[16], facial expressions[17], muscle activities[18], and human-prosthesis interface[4]. But they can only detect vibrations on the skin surface. Although vibrations in deep tissues can propagate to the skin surface if the vibration magnitude is large enough, like heartbeat, the vibration on the surface can only reveal very limited information, such as heart rate. Capturing more comprehensive information, such as the volume change of heart chamber, blood perfusion of aorta, and diaphragm contraction, requires direct accurate measurements of deep tissues.

- Optical sensors

Optical devices composed of light-emitting diodes (LEDs) and photodetectors emit light into tissues and measure reflected optical intensity. The reflected light intensity reveals the optical absorption and scattering properties of tissues. Usually, several LEDs at different wavelengths are used together to measure tissue properties, including blood oxygen saturation[1,19], cerebral hemodynamics[20], and blood pressure[21]. Because light diffuses in tissues, these devices only measure average properties of a tissue volume. Therefore, it is challenging to measure deep tissue properties with high-spatial resolution.

- Temperature sensors

Temperature sensors[1,2,4,19] based on electrical resistance changes are usually used to monitor the skin surface temperature. A dual temperature sensing[2] mechanism was applied for monitoring core body temperatures at a depth of ~1 cm. Temperature sensors based on photoacoustic technologies can noninvasively map temperature distributions at a depth of ~2 cm[22].

- Electrochemical sensors

Wearable electrochemical sensors continuously monitor the molecular components in biofluids, such as sweat[23], interstitial fluids[24], saliva[25], and tear[26]. Although these biofluids are only from the skin surface or shallow tissues, there are some correlations of molecular compositions between these biofluids and blood[27].

- Electrical impedance sensors

Electrical impedance tomography measures electrical impedances by an electrode array, which is suitable for noninvasive deep tissue monitoring. It is easy to be applied to monitoring large organs, like heart[28] and lung[29]. The spatial resolution is positively correlated to the number of electrodes for electrical impedance imaging. Therefore, a large number of electrodes are usually required to improve the spatial resolution, which increases the complexity and form factor of the whole system.

- Ultrasound sensors

Ultrasound transducers actively emit ultrasound waves into tissues and receive reflected waves for deep tissue sensing. Biomedical ultrasound waves usually have a short wavelength of tens to hundreds of micrometers, leading to high spatial resolution. Wearable ultrasound transducer arrays have high penetration depth (more than 14 cm) and high spatial resolution (better than 1 mm), as shown in the applications of monitoring central blood pressure[30], blood flow[31,32], heart chamber motion[33], hemoglobin distribution[22], and tissue modulus[34].

Supplementary Note 2 | Generation and stochasticity of surface EMG signals

A motor unit is the smallest system controlling muscle contraction. One motor unit is composed of a motor neuron, a neuron axon, and muscle fibers connected to axon branches[35]. The brain controls muscles by sending an electrical signal through the upper motor neuron to the spinal cord, the lower motor neuron, and finally the muscle fiber, causing muscle contraction. One motor unit firing instance means the motor unit receives a signal from the brain. Because one motor unit contains multiple muscle fibers, summation of electrical potentials of all muscle fibers is the motor unit action potential. Finally, an EMG signal is the algebraic summation of action potentials of fired motor units.

Surface EMG electrodes can noninvasively measure the EMG signals through electrolytic conduction, where the current can flow from tissues to the electrodes[36]. The surface EMG signal measured by an electrode on the skin surface can be mathematically modeled as[37]:

$$x(t)=\sum_{i}^{N}m_i(t)=\sum_{i}^{N}\sum_{j}^{M_i}\delta(t-t_{ij})*s_i(t)+n(t).$$

(1)

$x(t)$ is the measured surface EMG signal; t is the time; $m_i(t)$ is the action potential trace of the i^{th} motor unit, which is the temporal convolution between the firing instant $\delta(t-t_{ij})$ and the action potential waveform $s_i(t)$ of the i-th motor unit; $n(t)$ is the noise; t_{ij} is the moment of the j-th firing instance of i-th motor unit; N is the number of motor units; and M_i is the number of firing instances of the i^{th} motor unit. The firing rate of a motor unit and the number of fired motor units are both random. These factors make the surface EMG signal $x(t)$ inherently random for different measurements. Furthermore, the action potential waveform is bi-phasic or tri-phasic, which means it has both positive and negative phases[35]. Because of the randomness of firing of each motor unit and a low level of synchronization of firing between different motor units, the algebraic summation of motor unit action potentials could cause in-phase (enhancement) or out-of-phase (cancellation) summation. This also makes surface EMG signals inconsistent for different measurements.

Supplementary Note 3 | Can surface EMG measure signals from deep muscles?

Surface EMG is a non-invasive method that assesses the electrical activities of muscles by using electrodes placed on the skin surface. The efficacy of surface EMG in measuring signals from deep muscles is reliant on a variety of factors, including the size and location of the muscle, the thickness and conductivity of the surrounding tissues (such as skin and fat), and the attributes (such as the impedance, size) and placement of the electrodes. In general, surface EMG is more suitable for measuring signals from superficial muscles located near the skin surface, because the signals of electrical activities of deeper muscles are often attenuated by the overlying tissues. Nonetheless, through appropriate electrode placement and signal processing techniques, it may be possible to obtain useful surface EMG signals from certain deep muscles.

Supplementary Note 4 | Limitations of current soft wearable ultrasound transducer arrays

Soft wearable ultrasound transducer arrays with non-constraining integration on the human body allow continuous monitoring of deep tissues[30,31]. An array with many ultrasound transducers can provide more detailed information of muscles than one single transducer, which can further enhance the functionality, such as improving the accuracy of hand gesture tracking. However, a soft transducer array has uncertain morphologies when integrated on curved dynamic skin surface, resulting in unknown locations and orientations of the transducer elements in the array and thus inaccurate beamforming[31]. In addition, these arrays are still tethered to external bulky electrical controlling systems through wires, which would largely limit the subject mobility in daily applications.

In this work, we designed and fabricated a compact electrical system that integrated a single transducer, an electrical circuit, and a battery, with all components encapsulated in soft silicone elastomer. We would like to bring to the community that the data from a single-transducer ultrasound device is sufficient to infer health status of some respiratory patient groups and to reveal the muscle distributions for human machine interface. The single-transducer ultrasound device substantially simplifies the circuit components, lowers power consumption, and reduces the burden of data collection and processing. The final device could be attached to the skin without any tethering wires, suitable for daily monitoring applications. Potential applications of the fully integrated soft wearable ultrasound system include continuous tracking of arterial wall motions at great depth as a surrogate for blood pressure, measuring the sizes and motions of cardiac chambers to assess the anatomical and functional abnormalities of the heart, and evaluating the bladder volume for timely warning of patients with urinary incontinence.

Supplementary Note 5 | Comparison of this study with our previous work

The uniqueness of this device compared to our previously reported works can be summarized in terms of transducer array design, system integration level, applications, and deep learning algorithm, as shown in the Supplementary Table 1. Details are discussed below:

(1) Our previous research focused on fabricating ultrasound devices with multiple channels to achieve maximum signal quality and imaging capabilities. In this study, we demonstrate a device with a single transducer, substantially simplifying system complexity in terms of fabrication, circuitry, control logic, and device size, weight and power consumption while realizing health monitoring and human-machine interface simultaneously.

(2) Our previously reported device mainly focused on the ultrasound patch itself. A bundle of signal wires was required to connect the patch and the electrical controlling system, which limited the mobility of ultrasound patches. In this work, leveraging the small form factor of single ultrasound transducer and low burden of data, we specifically developed a fully-integrated circuit for driving the ultrasound transducer and collecting the data. This makes the wireless ultrasound system provide much enhanced mobility to wearers.

(3) Our previous applications primarily focused on biomedical applications such as blood pressure and flow monitoring, heart and brain imaging, and elastography. In this work, we demonstrated that this device can be used for two main applications. First, it can monitor the breathing patterns by tracking diaphragm movements in both healthy subjects and patients with respiratory diseases. Second, the device could be used as a human-machine interface by continuously tracking the hand gestures by analyzing ultrasound radiofrequency signals.

(4) In our previously reported works, deep learning algorithms were applied for segmenting and classifying processed ultrasound images. In this study, we demonstrate the deep learning algorithms can extract rich information from raw radiofrequency signals of only one

single transducer, establishing the connection between muscular ultrasound signals and hand gestures. Therefore, we extend the application scenarios of deep learning in ultrasound signal analysis.

Supplementary Note 6 | Interference sources in the signals and methods to mitigate them

Electromagnetic interference (EMI) in ultrasound systems can be classified into two main categories according to their frequencies: out-of-band noise and in-band noise. To attenuate EMI outside the frequency band of interest, we can use either analog or digital filtering[38]. Sources of such interference commonly include power lines and wireless communication devices like Bluetooth, Wi-Fi, and radio transmitters.

To attenuate EMI that falls within the frequency band of interest, the efficacy of conventional filters is substantially reduced. There are two main EMI sources in this band. First, EMI can be generated by the switching voltage regulators on the integrated PCB. These regulators adjust the voltage by rapidly toggling transistor switches, which operate at or near the ultrasound's operational frequency range and can handle substantial electrical currents, producing substantial EMI. To mitigate this, we physically separated the regulators from noise-sensitive components such as ultrasound transducers and amplifiers. In addition, we temporally separated switching operation from signal receiving and amplification. The switching regulators are deactivated in the ultrasound transmit/receive period (Fig. 2b). When the transmit/receive is finished, the switching regulators are activated again to charge the pulser. Second, other devices in the testing environment, such as wireless chargers and near-field communication systems operating within the megahertz range, may interfere with the ultrasound frequency band.

Because there were not these kinds of devices in our testing environment, such EMIR source is negligible.

Supplementary Note 7 | Comparison of our wearable ultrasound patch with other reported wireless sensors

Our echomyography device has three key advantages compared to the reported sensors in the literature.

First, most of the reported sensors typically involve rigid bulky circuits lacking flexibility[39-41]. This makes it challenging to conform to highly curved, dynamic body surfaces, introducing irritation and uncomfortableness to the skin for long-term wearable applications. In contrast, our system is built on flexible printed circuit boards and engineered with soft packaging, allowing it to conform seamlessly to the human skin. Our design and fabrication techniques can ensure reliable attachment, ultrasound coupling, signal fidelity, and comfort of wearing.

Second, some of the reported sensors still focus on the skin surface sensing. Typically, a wearable lung volume monitoring sensor integrated two polyvinylidene fluoride (PVDF) transducers for independent ultrasound emission and receiving[42]. The generated ultrasound wave propagates on the chest skin surface. Detecting the distance between the two PVDF sensors could infer the lung volume, similar to what a resistance-based strain sensor does[43]. Therefore, this kind of device does not directly capture the deep tissue information. In our work, we applied PZT 1-3 composite as the piezoelectrical transducer whose ultrasound wave penetrates several centimeters below the skin surface. Hence our device can directly capture deep tissue information and provide a high spatial resolution.

Third, previously reported wireless ultrasound sensors rely on traditional signal processing methods, which inherently limit their capabilities and applications. Wearable ultrasound sensors can be based on A-mode to reduce the burden of data collection, transmission, and processing. However, in this case the acquired data is only suitable for distance detection of tissue interfaces. For example, bladder volume can be inferred by sensing the distance between the anterior and posterior walls of the bladder. In this work, we developed deep learning algorithms to analyze the signals from a single-channel transducer and extract much more information than only the distance. Specifically, we demonstrated deep learning algorithms could infer the hand gesture from only one radiofrequency signal trace, which could be used as a wearable human-machine interface. This work is qualitatively different in the data processing methods and applications of wearable ultrasound sensors from the other studies.

Supplementary Note 8 | Bland-Altman analysis

Bland-Altman plot analyzes the agreement between two groups of datasets captured by two measurement techniques. This plot has been widely used in analytical chemistry and biomedicine[44] to compare a new measurement method with the gold standard. *X* and *Y* are the datasets measured by the two methods. The *x*-coordinate of Bland-Altman plot is the average of *X* and *Y* while the *y*-coordinate is the difference between each paired *X* and *Y*. In Bland-Altman plot, there are three horizontal lines, representing the mean bias $\bar{d}$, the upper limit of agreement E_{upper} and the lower limit of agreement E_{lower}. They are calculated as:

$$\bar{d} = \frac{1}{n}\sum_{i=1}^{n}\left(Y_i - X_i\right) \tag{2}$$

$$E_{lower} = \bar{d} - 1.96 \times sd \tag{3}$$

$$E_{upper} = \bar{d} + 1.96 \times sd \tag{4}$$

where *sd* is the standard deviation. 1.96 is the boundary for the 95%-confidence interval in a standard normal distribution.

Supplementary Note 9 | Techniques for recognizing and tracking hand gestures

Recognizing hand gestures means differentiating limited number of specific discrete hand gestures based on measured signals. However, tracking hand gestures requires measuring the bending angles of finger joints and the rotation angles of the wrist continuously. Tracking hand gestures is not limited to several specific discrete gestures, but involves continuously monitoring the angles of finger bending and wrist rotating for each specific discrete hand gesture[45]. There are several techniques for recognizing discrete and tracking continuous hand gestures, including computer vision[46-48], strain sensing[6,49,50], IMU sensing[51], electromyography[52], and ultrasonography[53-55].

- Computer vision

Computer vision uses cameras to acquire photos or depth images of the human body and process them with machine learning algorithms. It can continuously track the motion of fingers and wrist without the need for wearing any sensors. However, the hand can sometimes be occluded by other objects, and the fingers can block each other from the camera. A potential solution is to detect the gesture from multiple views by combining multiple cameras, which increases the cost and complexity of the system. Because the cameras are usually bulky and not portable, this method is not always applicable if the hand is not within the view of cameras. In addition, the light in surrounding environment has a strong influence on the tracking accuracy.

- Strain or IMU sensor-based gloves

Many studies also developed wearable gloves to track the motion of fingers and wrist[56-58]. Researchers usually install a strain sensor on each finger joint to measure the bending of the joints, then the hand gesture can be depicted after the angles of all finger joints are determined. They may also use IMU sensors to measure the movements of fingers and the palm in the 3D space. These wearable gloves can work at any position and in any light environment. But they need many sensors to track the configuration of one hand, resulting in complex wire connections and a large device form factor. Furthermore, gloves are totally inapplicable for amputees.

- Surface EMG

Surface EMG is another widely used technique for recognizing and tracking hand gesture. Surface EMG electrodes detect electrical potential generated by motor units, traveling along muscle fibers[52]. However, surface EMG signals are weak and have low signal to noise ratio during low-level muscle activation, resulting in low classification accuracy for discrete hand gestures[59]. Previous studies have also demonstrated the low accuracy of surface EMG signals for recognizing different facial expressions[12].

- Ultrasonography

As a convenient way to detect muscle activities, ultrasonography has also been demonstrated in recognizing hand gestures[53-55]. Ultrasound can penetrate deeply into tissues and noninvasively image muscle groups during hand motion, including deep muscles that are inaccessible for surface EMG electrodes. However, previous studies by fixing bulky ultrasound probes on the forearm with rigid fixtures are not user-friendly because of the large volume and weight of the setup[53-55]. Furthermore, these studies only demonstrated classifying several specific discrete gestures, unable to track dynamic hand gestures continuously.

In this work, we designed and fabricated a fully integrated single-channel echomyography (EcMG) system, which is composed of a compact single ultrasound transducer, a flexible printed circuit board (fPCB) for transducer activation and wireless data communication, and a lithium-polymer battery. The ultrasound system has a small form factor and soft mechanical interface with the skin, making it wearable and user-friendly. The system can continuously measure the motion of muscle groups in the forearm (and other body parts). We also developed a deep neural network to analyze the radiofrequency (RF) data of the single transducer to track the dynamic finger and wrist motions with high accuracy in real time.

Supplementary Note 10 | Frame rate of hand gesture tracking using EcMG

One ultrasound RF signal has a time duration of several tens of microseconds. We can acquire thousands of such RF signals in one second in principle. Each RF signal can be used to predict one hand gesture. So, EcMG can theoretically achieve a frame rate of thousands of Hz. In consideration of the fact that hand gesture does not change too fast, and a lower frame rate can lower the data acquisition frequency and thus power consumption, we designed the system with a frame rate of 50 Hz.

Supplementary Note 11 | Detection depth and data acquisition time

For detecting forearm muscles, we recorded 1024 sampling points per RF signal. Because the sampling rate is 12 MHz, the corresponding data acquisition time is about 1024/12 MHz $\approx$

85 μs. In consideration of the sound speed of about 1540 m/s, the nominal detection depth is about 6.6 cm. The typical thickness of forearm muscles is <6.6 cm. However, because ultrasound waves could experience multiple reflections in the forearm, we could record a signal with a nominal depth greater than the forearm thickness.

Supplementary Note 12 | Angle estimation based on the accelerometer and magnetometer

The IMU sensor (KMX62) in the commercial glove development kit in this work had a three-axis accelerometer and a three-axis magnetometer. Their outputs could be defined as X_{Acc}, Y_{Acc}, Z_{Acc}, X_{Mag}, Y_{Mag}, and Z_{Mag}. Then the roll and pitch angles could be easily calculated based on the following equations[60]:

$$Roll = atan2\left(\frac{Y_{Acc}}{Z_{Acc}}\right) \tag{5}$$

$$Pitch = atan\left(\frac{-X_{Acc}}{Y_{Acc}sin(Roll) + Z_{Acc}cos(Roll)}\right) \tag{6}$$

Function *atan*2 has an output angle range of -180° to 180°, while *atan* has an out angle range of -90° to 90°.

The magnetometer data were used to calculate the yaw angle. However, the magnetic measurement is usually affected by the magnetic field created by the surrounding environment. Assuming no distortion, the output of the magnetometer in three directions should form a spherical surface in the 3D space, with the origin at X_{Mag}=0, Y_{Mag}=0, and Z_{Mag}=0. The environmental magnetic field will shift the center of the sphere by a bias, while the shape of the sphere is maintained. In this work, we adopted a convenient way to eliminate the distortion of the surrounding environment[61]. We spun the IMU sensor in a spherical surface in the 3D space over 1000 periods and collected more than 10000 magnetometer outputs. The average values of the magnetometer in the *X*, *Y*, and *Z* directions were calculated as X_{Offset}, Y_{Offset}, and Z_{Offset}. Then the real magnetometer values were computed according to:

$$X_{Real} = X_{Mag} - X_{Offset} \tag{7}$$

$$Y_{Real} = Y_{Mag} - Y_{Offset} \tag{8}$$

$$Z_{Real} = Z_{Mag} - Z_{Offset} \tag{9}$$

The outputs of the magnetometer before and after the calibration are shown in Supplementary Fig. 21. Obviously, the calibrated magnetometer values were distributed on a spherical surface with the origin at X_{Mag}=0, Y_{Mag}=0, and Z_{Mag}=0. After the calibration, the yaw angle could be calculated by:

$$Yaw = atan2\left(\frac{Y_{Real}}{X_{Real}}\right) \tag{10}$$

However, this equation was only applicable when the sensor was flat, i.e., when the roll and pitch angles were both zero. It was impossible to maintain this condition all the time. Therefore, we compensated the influence of arbitrary roll and pitch by[61]:

$$Yaw = atan2\left(\frac{Y_{Real}cos(Roll) - Z_{Real}cos(Pitch)sin(Roll) + X_{Real}sin(Roll)sin(Pitch)}{X_{Real}cos(Pitch) + Z_{Real}sin(Pitch)}\right) \tag{11}$$

Supplementary Note 13 | Improving the accuracy and generalization capability with a transducer array

For the single transducer, the measured RF signal may change pronouncedly if the detect position changes. To improve the accuracy and generalization capability of this technology for continuous hand gesture tracking, we could extend the single transducer to a transducer array. In this case, the array does not need beamforming as conventional transducer arrays do, because here each transducer would work independently to acquire the RF signals from different angles/locations of muscles. A transducer array can capture multi-channel RF signals from multiple angles/locations, acquiring more comprehensive information of the muscle activity. Even the detection position of the transducer array changes, the multi-channel signals may still keep similar. Therefore, a transducer array could be less sensitive to the placement angles/locations of the transducers, having higher accuracy and generalization capability. Those RF signals from the transducer array could be fed into the deep neural network for processing separately.

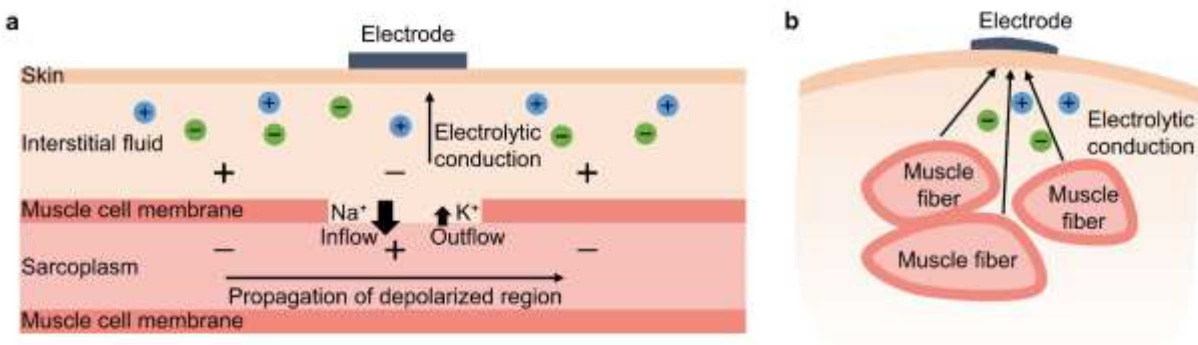

Supplementary Fig. 1 | Propagation of an action potential along and outside the muscle fiber. a, The excitation of a muscle fiber causes depolarization in the muscle cell membrane, which induces an inflow of Na^+, an outflow of K^+, and a potential change at that region[62]. The depolarization area will then be restored to the original state due to active ion pumping[63]. On one hand, the depolarization area travels along the muscle fiber, resulting in the propagation of an action potential. On the other hand, the action potential causes ions in the interstitial fluid to flow, i.e., electrolytic conduction, which can be captured by surface electrodes[36]. **b**, One surface electrode can collect such biopotentials from multiple muscle fibers in the vicinity and thus lack one-to-one correspondence and spatial resolution.

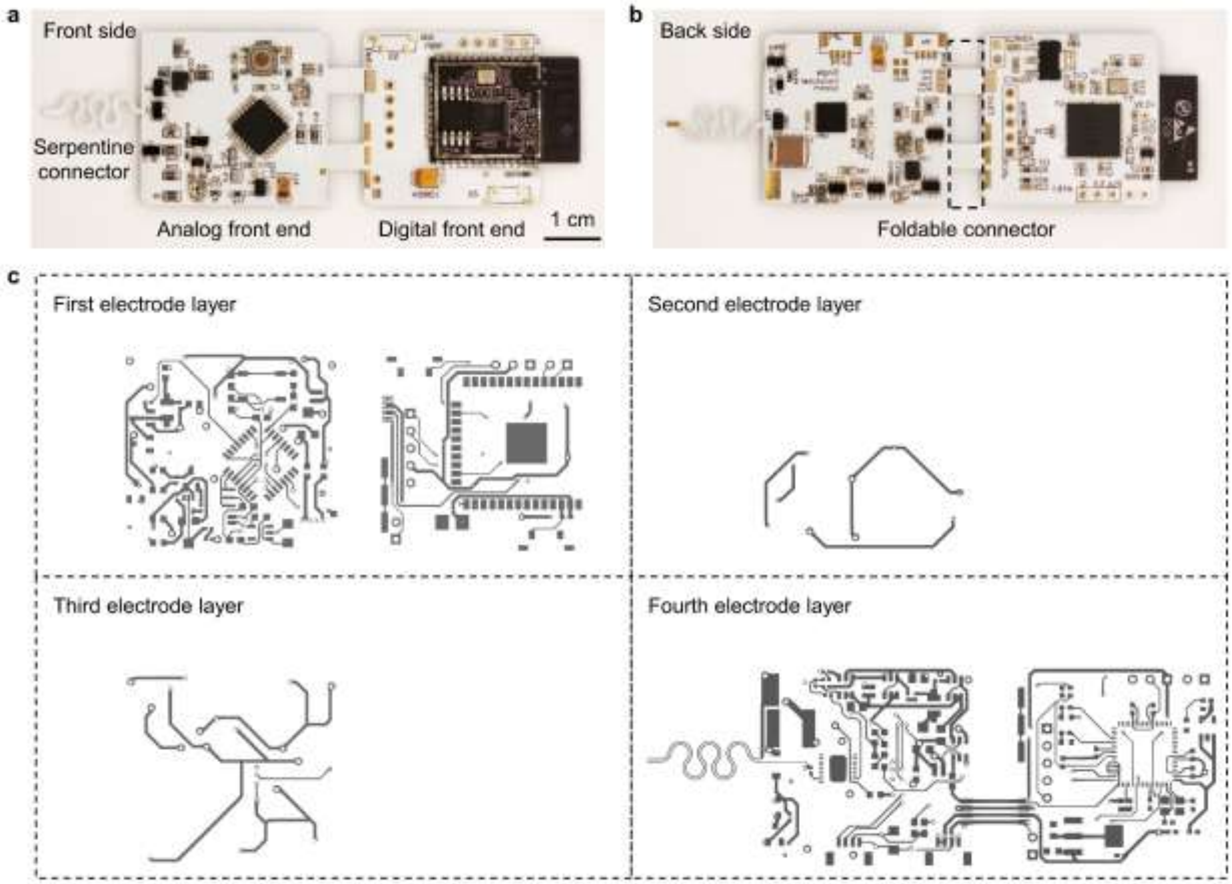

Supplementary Fig. 2 | Design and fabrication of the fPCB. a, Front side of the fPCB, which is composed of an analog front end and a digital front end. The serpentine connector links the circuit board to the single transducer. **b**, Back side of the fPCB. The two sub-boards are linked by a foldable connector. **c**, Four electrode layers of the fPCB to minimize its overall footprint.

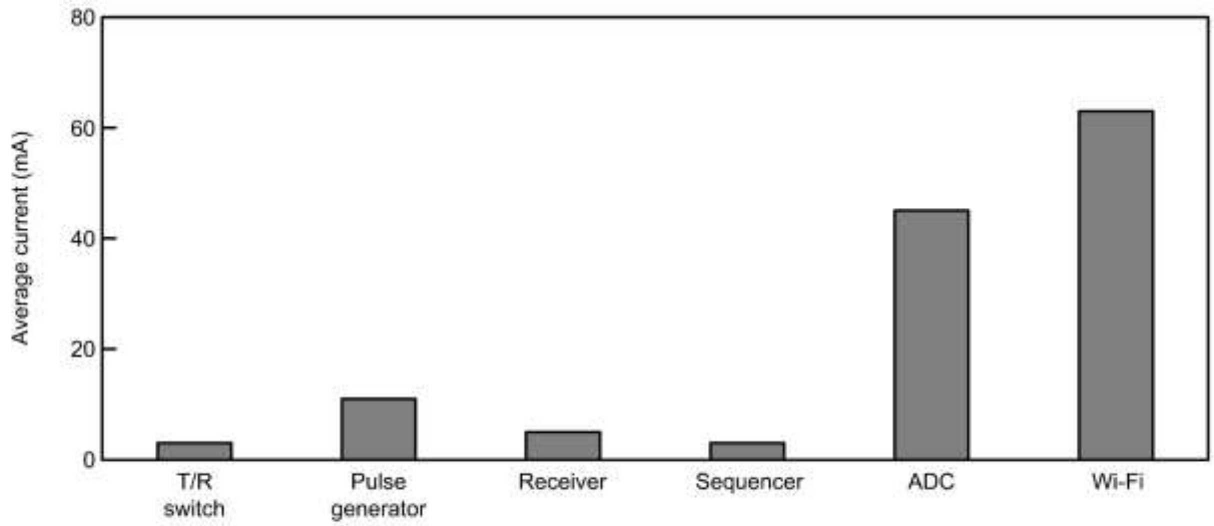

Supplementary Fig. 3 | Power consumption of key components in the fPCB. All components operate at 3.7 V. The Wi-Fi module transmits a group of data to the backend receiver every 20 ms to reduce the power consumption. T/R: transmit/receive. ADC: analog to digital converter. Our ultrasound system used a commercially off-the-shelf lithium battery as the power source, for which 3.7 V is a standard voltage. Because many chips (such as the operational amplifier ADA4895-1ARJZ-R7) can be powered in a range of supply voltages, a 3.7-V battery can directly power the chip. For some chips that 3.7 V is not suitable, we also integrated linear regulators in our PCB circuit, which transformed the 3.7 V to acceptable voltage levels.

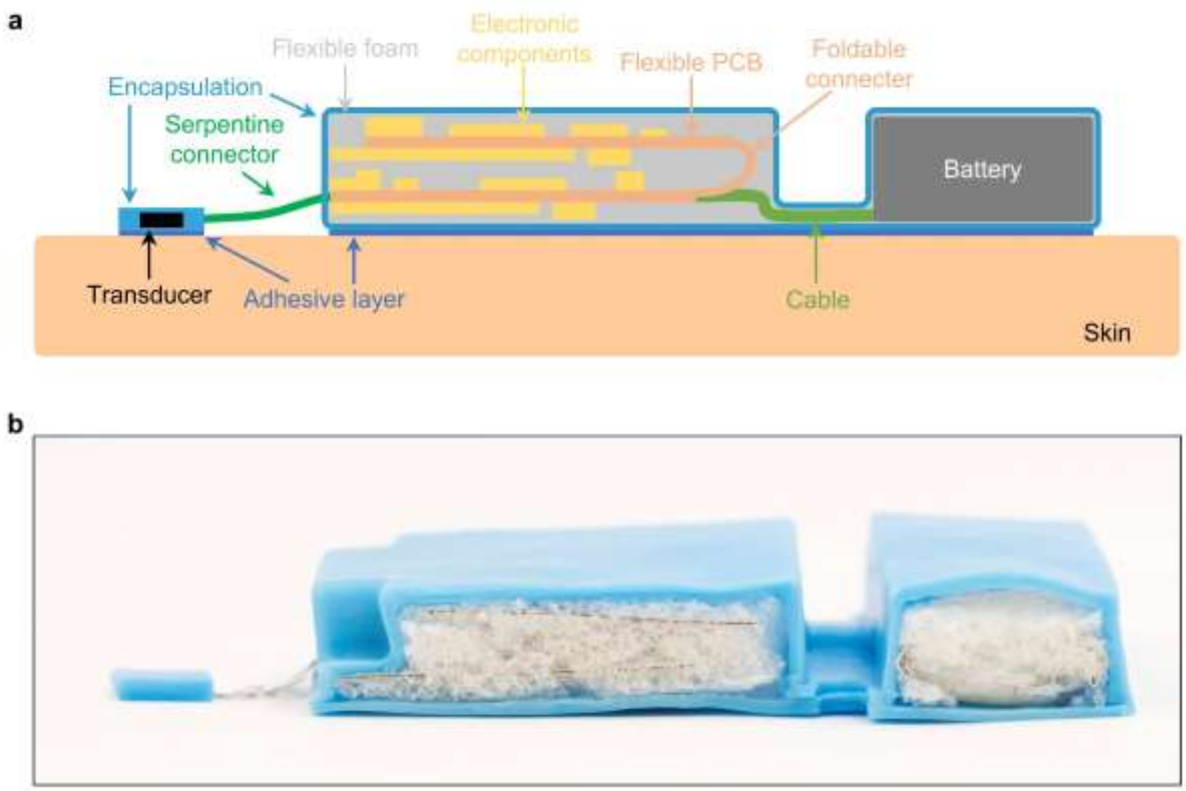

Supplementary Fig. 4 | Cross-sectional architecture of the wearable single-channel ultrasound system. a, Schematics of the cross section of the ultrasound system. The single transducer, fPCB, and battery are all encapsulated in silicone elastomer (Ecoflex 00-30). The patch is attached to the skin with a thin layer of adhesive silicone (Silbione). **b**, Image of the cross section of the ultrasound system.

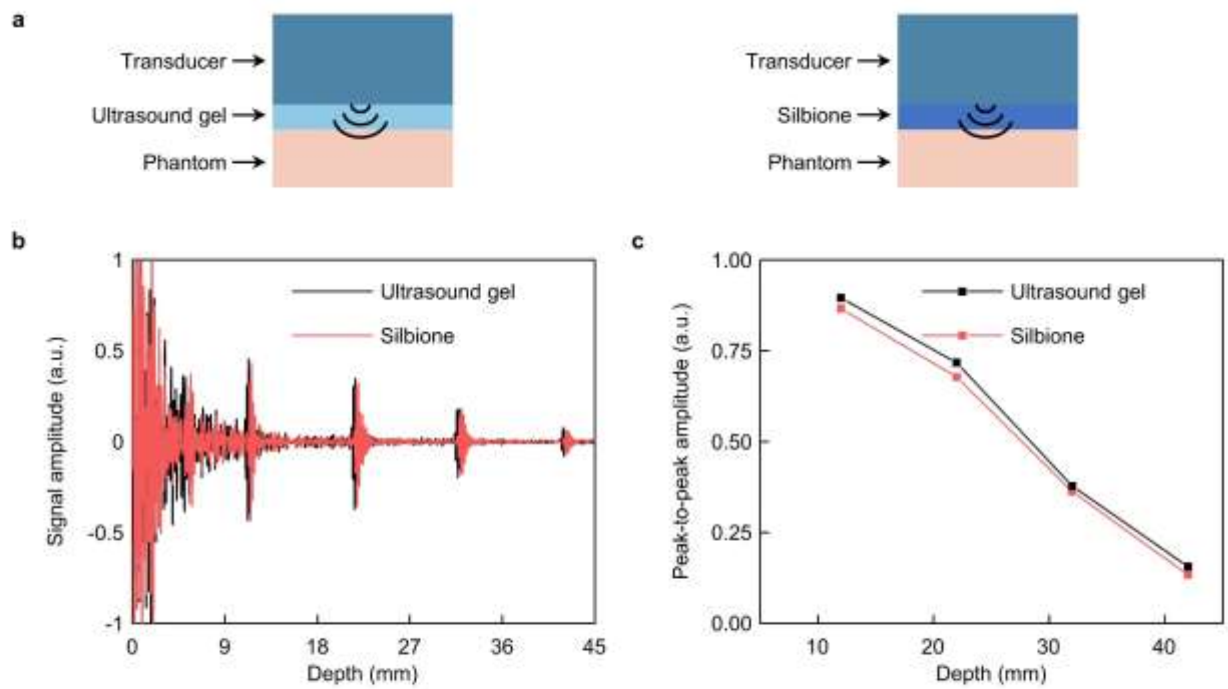

Supplementary Fig. 5 | Ultrasound coupling properties of adhesive silicone (Silbione). a, Schematics showing the comparison of ultrasound transmission properties between the ultrasound gel and Silbione adhesive layer. **b**, Ultrasound echo signals reflected by scatterers in a commercial phantom (CIRS, Model ATS 539) as measured using ultrasound gel and Silbione as the couplant. **c**, Peak-to-peak amplitudes of the signals in **b**. Their similar magnitudes reveal the similar coupling behavior of Silbione to ultrasound gel.

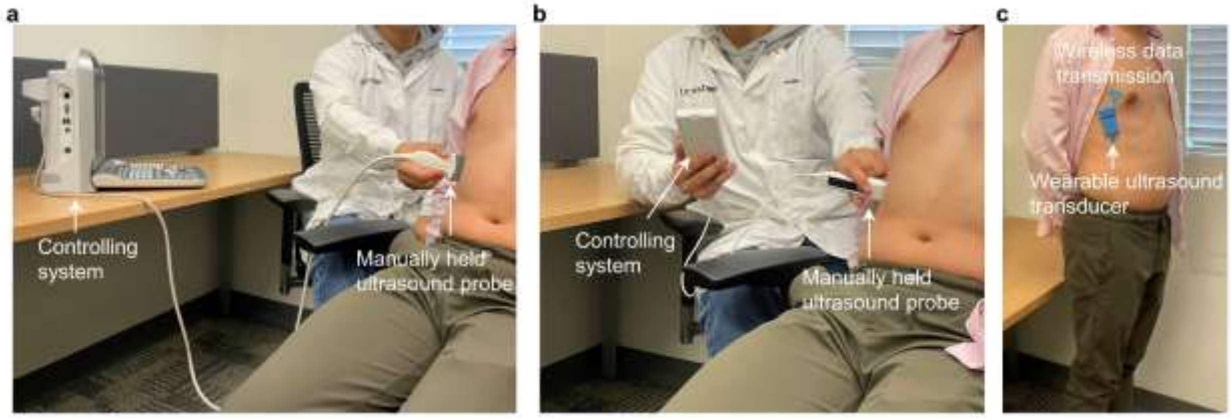

Supplementary Fig. 6 | Comparison among different ultrasound systems. a, A commercial portable ultrasound system with a laptop-sized controller. Operators need to manually hold the bulky ultrasound probe during examination. The subject needs to keep static to reduce the relative motion between the body and the probe. **b**, A commercial portable ultrasound system with a mobile phone-sized controller. Operators also need to manually hold the bulky ultrasound probe during examination and the subject must keep static to reduce any relative motion between the body and the probe. **c**, The fully integrated wearable ultrasound system demonstrated in this work. The entire system has a low form factor and can be attached to the skin without manual holding. The wireless operation substantially reduces restrictions to the human body.

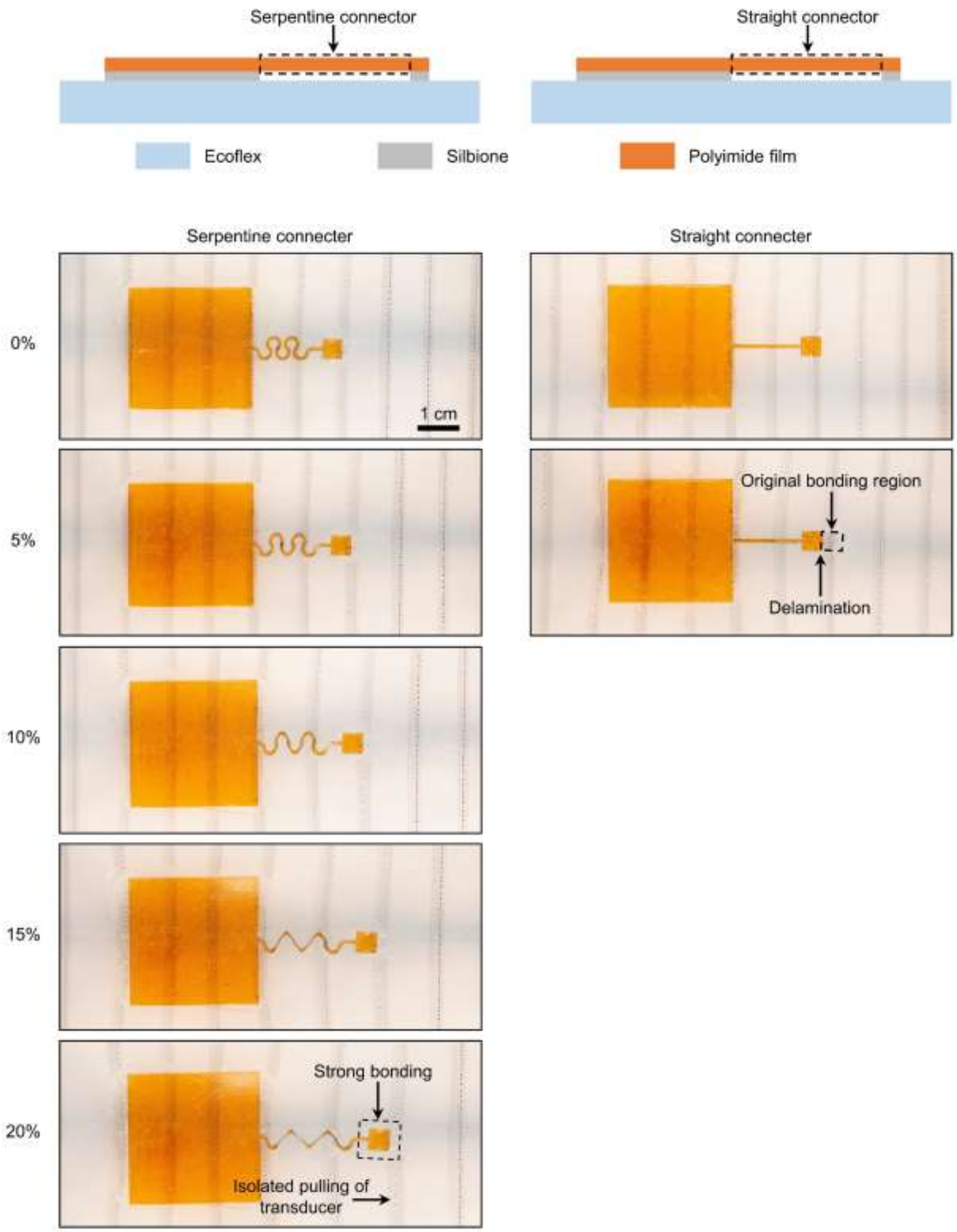

Supplementary Fig. 7 | Serpentine connecter of the fPCB for motion isolation. An Ecoflex substrate with a thickness of 3 mm was used to mimic human tissues. We fabricated two polyimide sheets with shapes similar to the fPCB and the single transducer. One of them has a serpentine connector while the other one has a straight connector. The Ecoflex substrate is bonded with the polyimide sheet with adhesive silicone (Silbione). For the serpentine connector, even if the substrate is stretched up to 20%, the smaller part, which mimics the single transducer, is not pulled by the larger part, which mimics the fPCB. The smaller part is still bonded with the substrate strongly, which means the motion of the fPCB has slight influence on the single transducer. But for the straight connector, the fPCB part has large influence on the single transducer. The delamination between the single transducer and substrate occurs even under only 5% stretching.

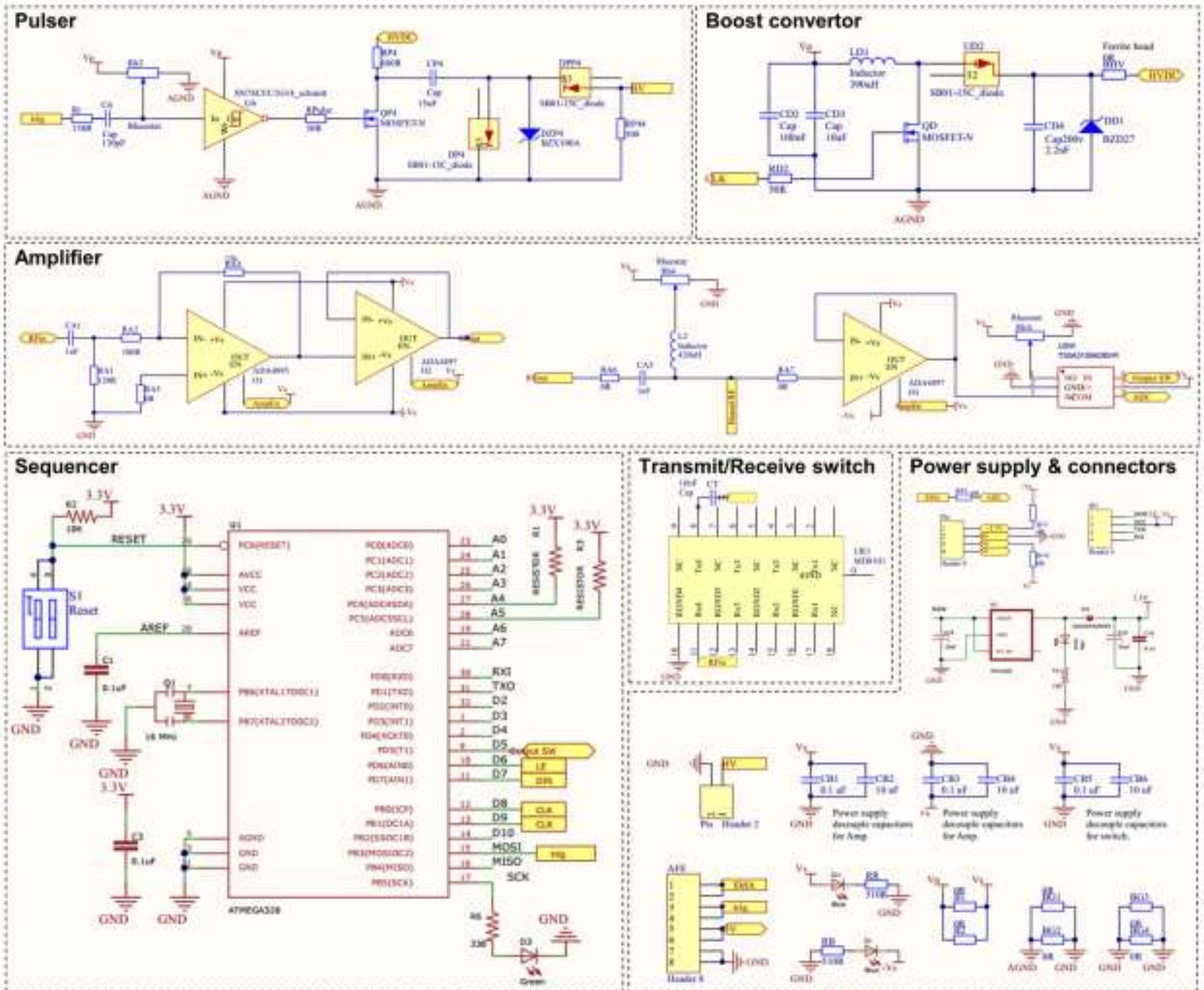

Supplementary Fig. 8 | Schematic circuit diagrams of the analog front-end components. The analog front end includes the pulser, boost convertor, amplifier, sequencer, transmit/receive switch, and power supply and connectors.

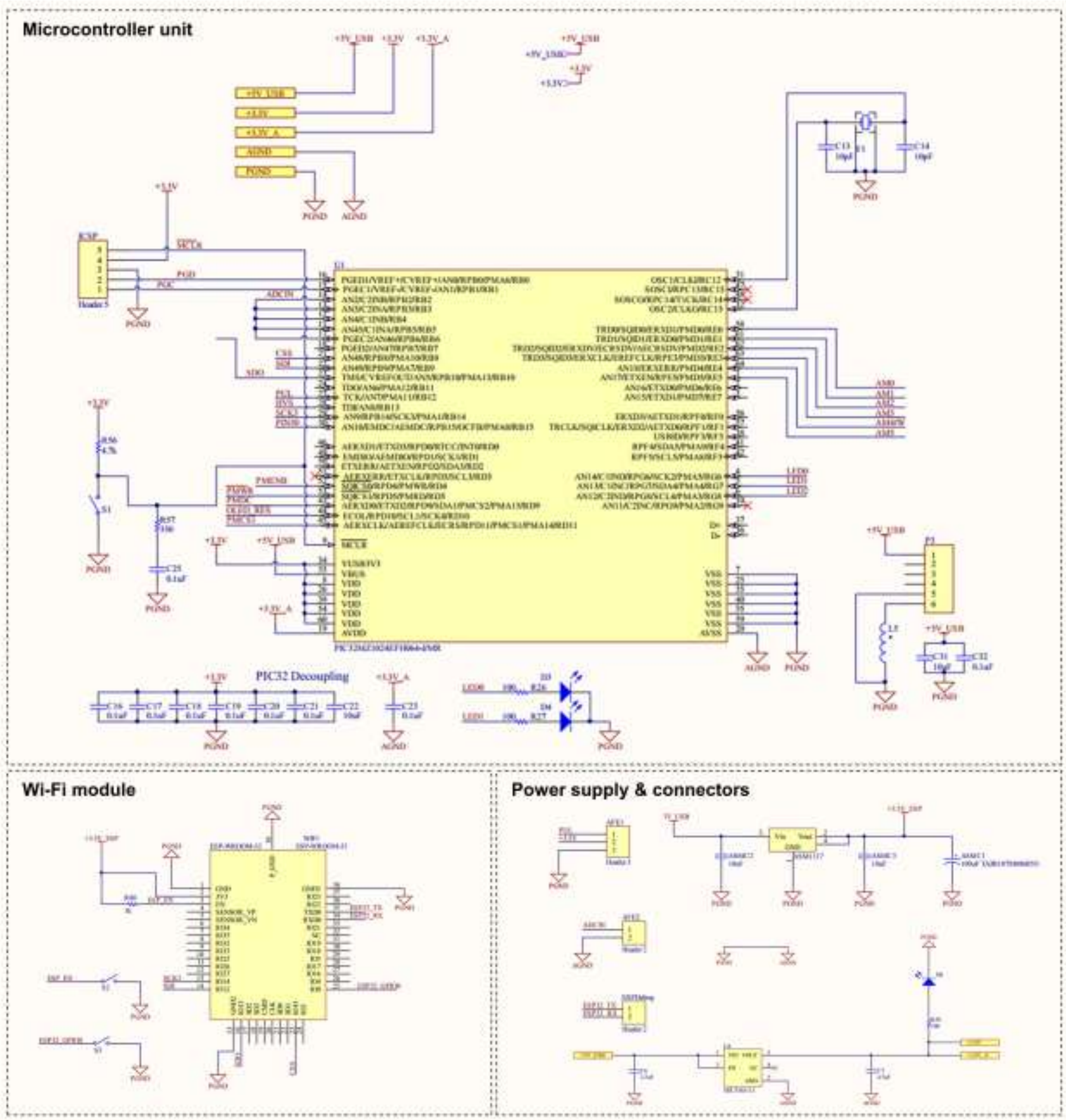

Supplementary Fig. 9 | Schematic circuit diagrams of the digital front-end components. The digital front end includes the microcontroller unit, Wi-Fi module, and power supply and connectors.

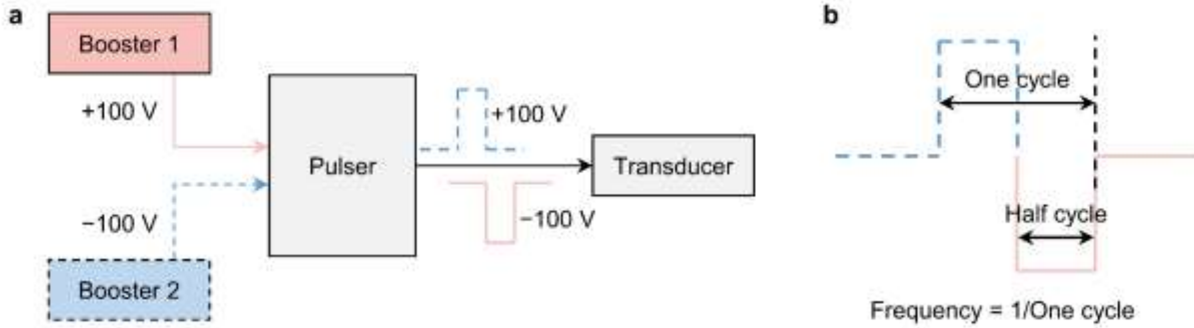

Supplementary Fig. 10 | Schematic illustration of high-voltage driving pulses. a, The booster circuit provides high direct current voltage to the pulser circuit, which then generates a high-voltage pulse wave to drive the transducer. Two booster circuits are required to provide bipolar high voltages, if a bipolar pulse wave is needed. In this work, we only integrated one booster for the positive high voltage supply. Then the pulser circuit only drives the transducer with a negative high-voltage pulse. Both a full cycle and a half cycle pulses can be used to drive the transducer. The half cycle pulse could result in a lower signal amplitude but higher signal bandwidth than the full cycle pulse. **b**, For the bipolar pulse, the frequency equals 1/one full cycle duration. For the half cycle used in this work, the frequency still equals 1/one full cycle duration.

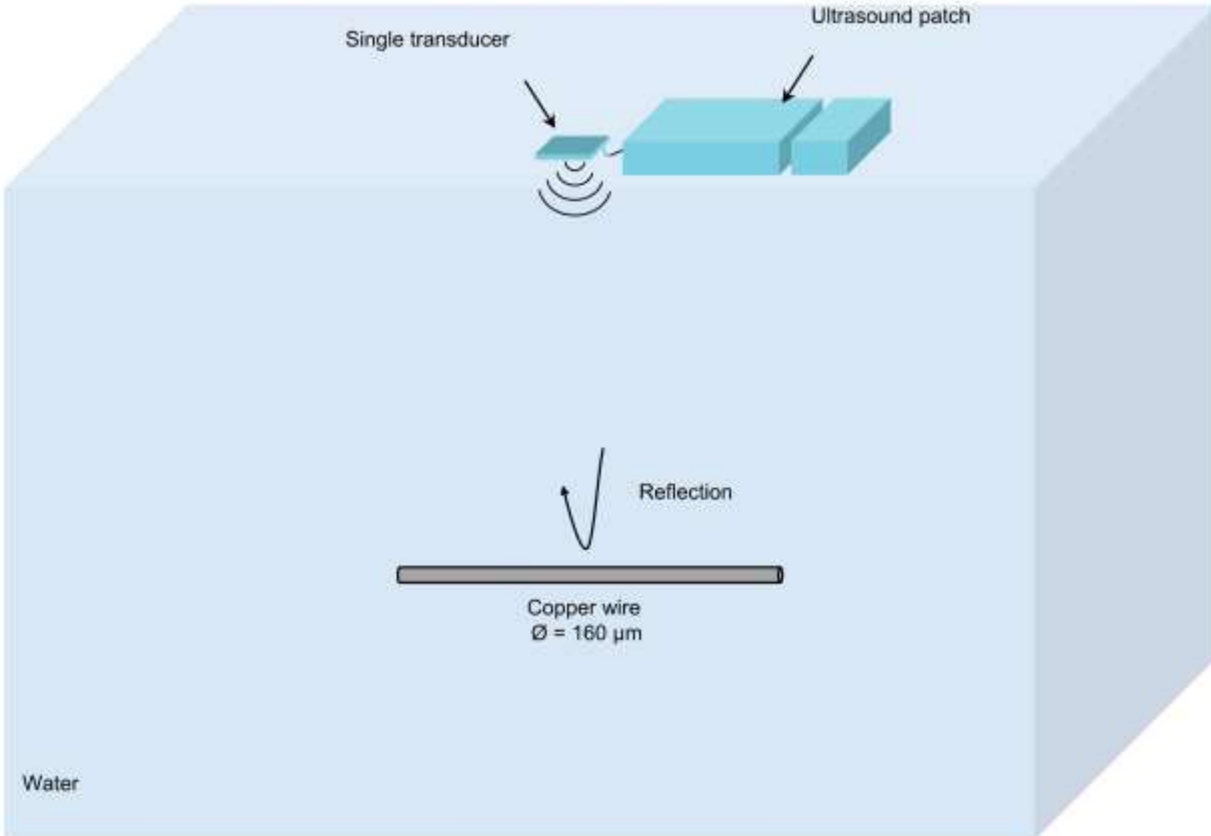

Supplementary Fig. 11 | Impulse response measurements of the single-transducer ultrasound system. The single-transducer ultrasound system is supported on the water surface. It emits a pulse wave in the direction perpendicular to a copper wire (diameter = 160 μm), receives the echo signal, and wirelessly transmits the received signals to a computer for further processing.

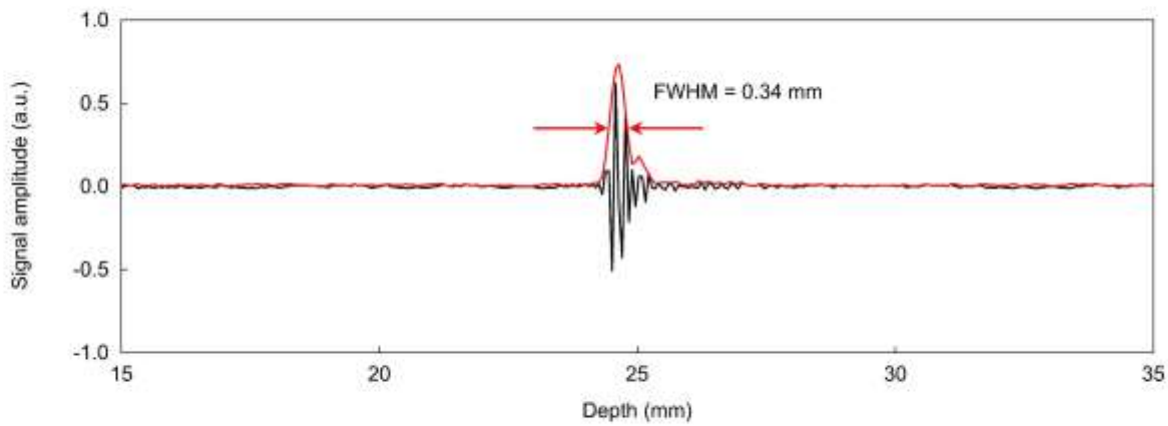

Supplementary Fig. 12 | Characterization of the axial resolution. The spatial resolution is an important metric that characterizes the accuracy of diaphragm thickness measurements. Because our ultrasound system operates at the A-mode, which reflects the dimensions of tissue layers at different depths, the axial resolution represents the spatial resolution of our system. We measured the pulse echo signal of one thin copper wire (diameter = 0.16 mm). The full width at half maximum (FWHM) was calculated from the signal envelope to be 0.34 mm. Therefore, the axial resolution of our system is 0.34 mm.

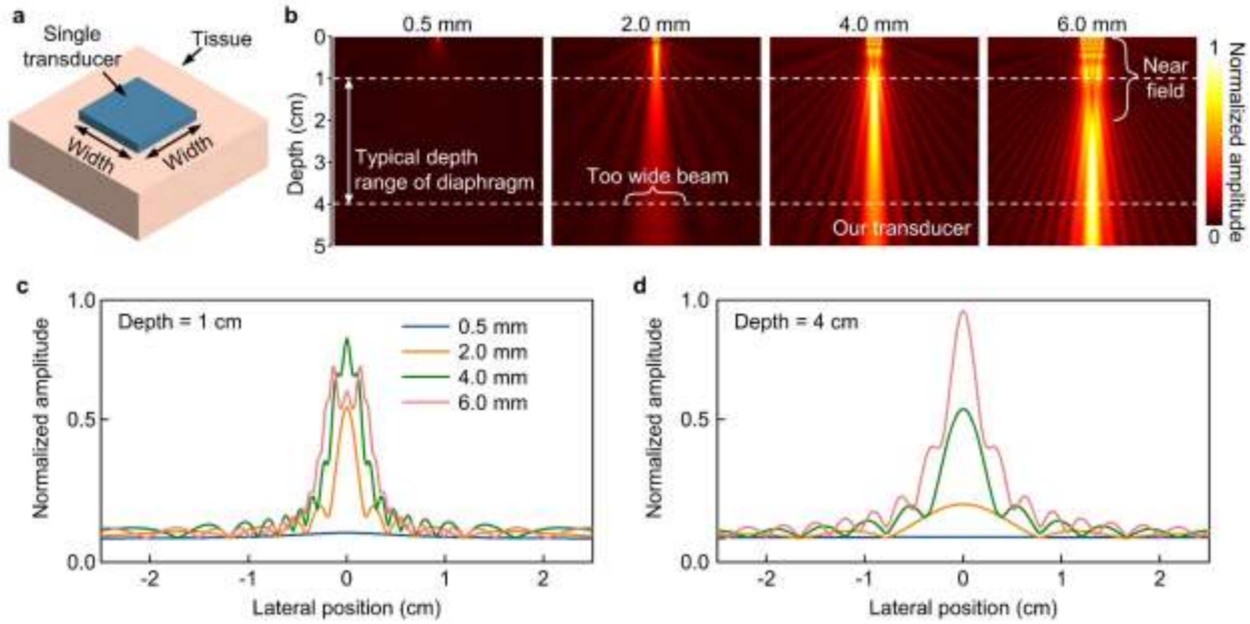

Supplementary Fig. 13 | Simulated sound fields of single transducers with different sizes. a, Schematics of the single transducer on a tissue surface. **b**, Simulated sound fields in the vertical plane of different single transducers. The widths of square single transducers are 0.5 mm, 2.0 mm, 4.0 mm, and 6.0 mm. When the width is small, e.g., 0.5 mm and 2.0 mm, the sound beam is too wide at great depth. When the width is large, e.g., 6.0 mm, the near field of the single transducer is too long. Amplitudes of ultrasound waves fluctuate greatly in the near field region. Ideally, the sound beam should be narrow in the typical diaphragm depth range from 1 to 4 cm. Therefore, 4 mm is selected as the transducer width in this work. **c**, Sound field profiles of the transducers of different widths at the depth of 1 cm. **d**, Sound field profiles of the transducers of different widths at the depth of 4 cm.

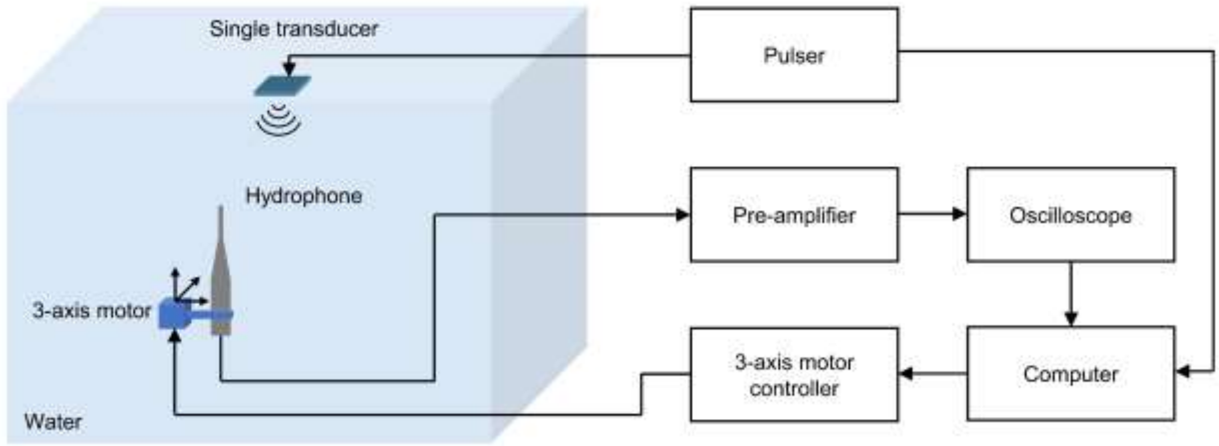

Supplementary Fig. 14 | Schematics of the sound field scanning system. A pulser (Olympus, 5077PR) emits a pulse voltage with an amplitude of 100 V to excite the single transducer. The ultrasound wave emitted from the single transducer is received by the hydrophone (ONDA, Model no. HNP-0400), amplified by the pre-amplifier, digitized by the oscilloscope (PicoScope 5000), and then recorded by the computer. The pulser sends a trigger signal to the computer to synchronize the wave transmission and receiving. The peak-to-peak value of the received signal is extracted as the sound field amplitude at the scanning point. A three-axis motor controlled by the computer moves the hydrophone to map the sound field in the 3D space.

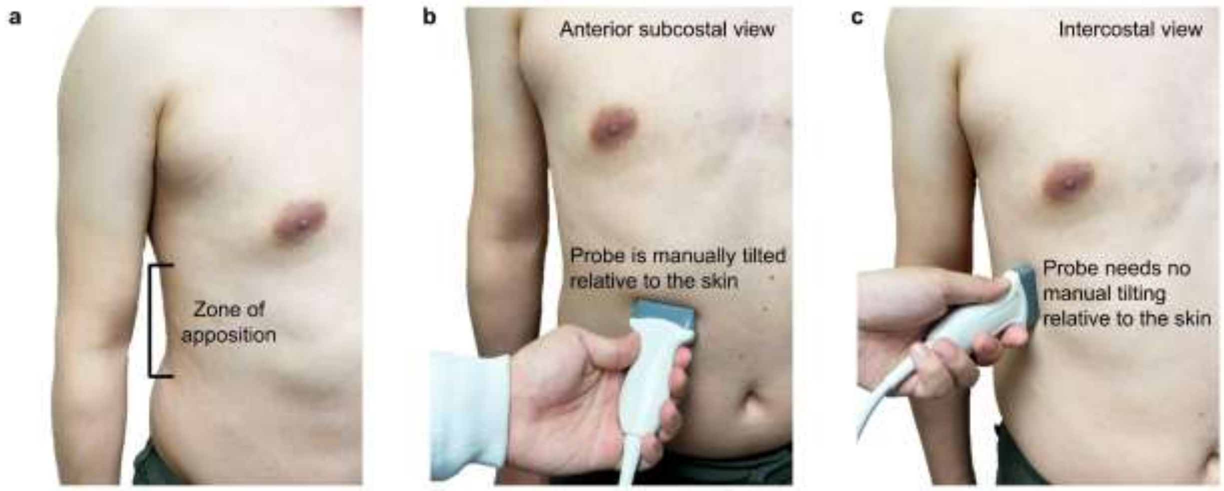

Supplementary Fig. 15 | Different modes of detecting the diaphragm. **a**, The zone of apposition is the vertical area that is directly behind the inner aspect of the lower chest wall and the rib cage. Anterior subcostal view and intercostal view within the zone of apposition are widely used for diagnosing diaphragm in clinics. **b**, An ultrasound probe can detect the maximum diaphragm displacement during breathing from the anterior subcostal view to assess the inspired volume[64]. But the ultrasound probe needs to be manually tilted to make sure the ultrasound beam goes towards the diaphragm, which is not practical for hand-free long-term monitoring. Moreover, this view only reveals the lung volume during the inspiratory phase, incapable of differentiating the contributions from assistive devices (e.g., a mechanical ventilator) or the subject's diaphragmatic contraction[65]. **c**, An ultrasound probe detects the diaphragm thickness from the intercostal view. The probe can be held vertical to the skin for examination, without manual tilting. This view is suitable for hand-free wearable ultrasound applications.

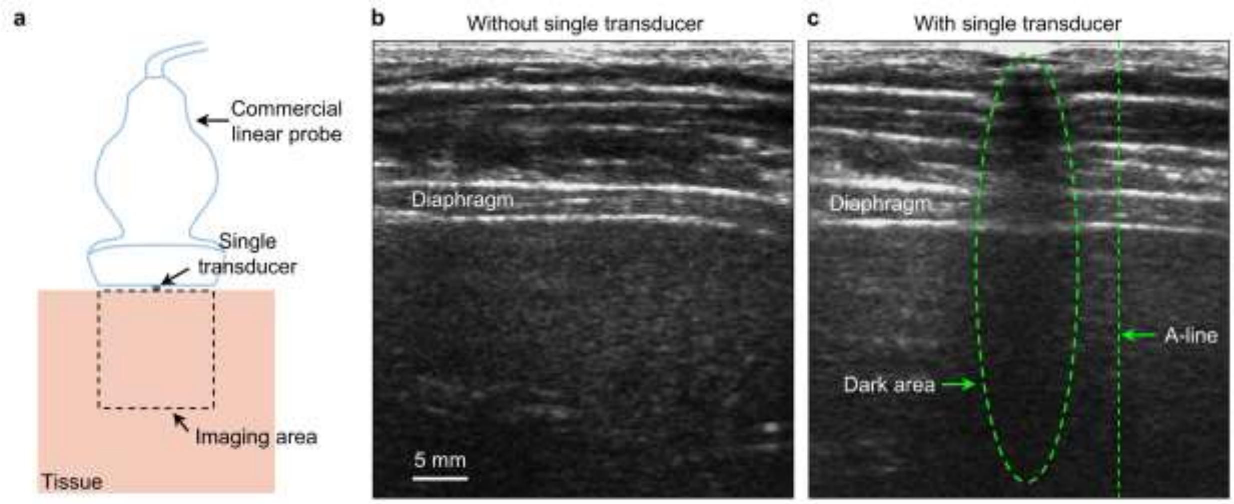

Supplementary Fig. 16 | Simultaneous measurements of the diaphragm with the single-transducer system and a commercial probe. a, Schematics of placing a commercial probe on the single-transducer system to simultaneously measure the diaphragm. **b**, If the single-transducer system is absent between the tissue and the commercial probe, the commercial probe can get a clear B-mode ultrasound image. **c**, If the single-transducer system lies between the tissue and the commercial probe, it blocks a small portion of the commercial ultrasound probe. Therefore, there is a dark area in the B-mode image of the commercial probe, underneath the position of the single transducer. An A-line in the B-mode image, which has a slight horizontal offset (~1 cm) to the single transducer, is extracted to compare it with the measurement of the single transducer. The diaphragm is parallel to skin judging from the B-mode image. Therefore, the ultrasound beam vertical to the diaphragm can detect the diaphragm thickness accurately.

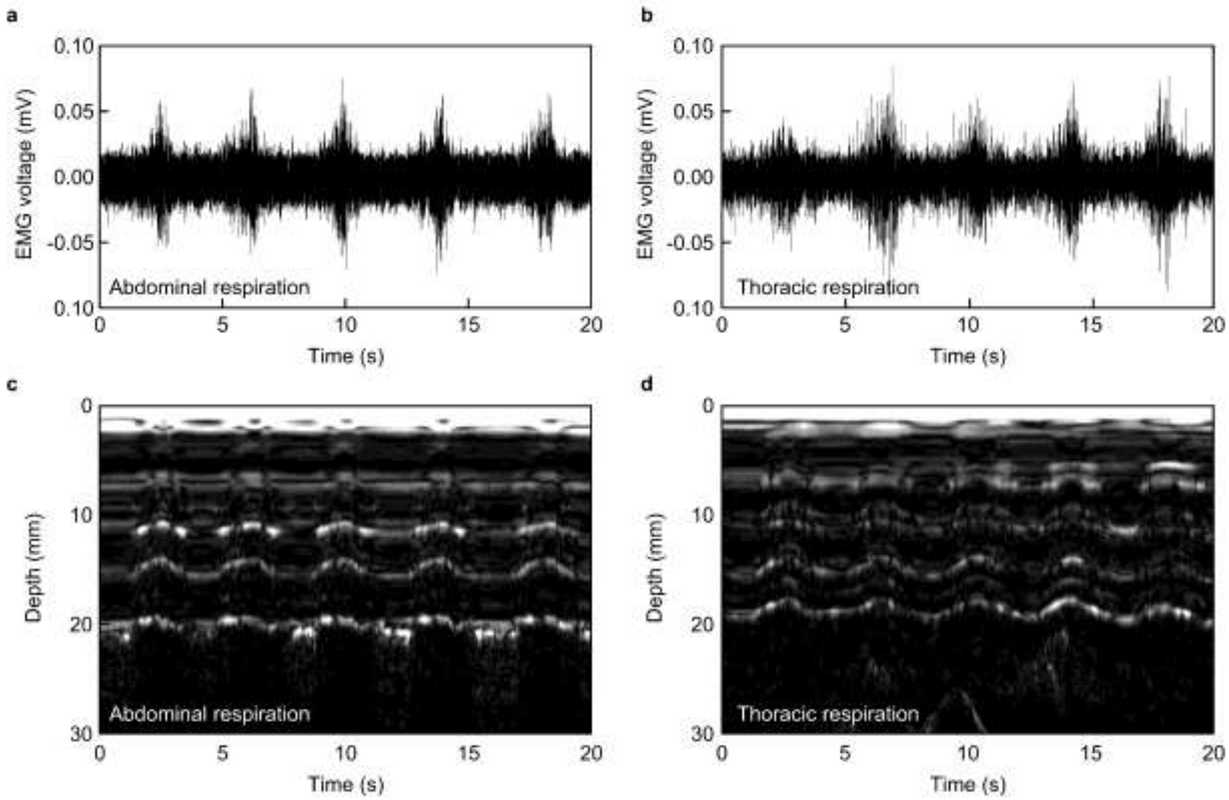

Supplementary Fig. 17 | Comparison between conventional electromyography and our echomyography for diaphragm monitoring. EMG signals during (**a**) abdominal and (**b**) thoracic respirations. Ultrasound signals during (**c**) abdominal and (**d**) thoracic respirations. A volunteering participant did abdominal and thoracic respirations for several tens of seconds. In the meantime, we recorded the EMG and ultrasound signals of the diaphragm using BioRadio and our wearable ultrasound system. The raw EMG signal was filtered by a 60 Hz notch filter and a 100~500 Hz bandpass filter. Such a bandpass filter was used because the surface EMG signals were mainly in this frequency band[66]. Because the surface electrodes capture signals from all muscles, the EMG signals are the mixture of all of them. It is challenging to recognize the diaphragm activity because other muscles could have also contributed to some of the EMG signals. However, the wearable ultrasound system directly measures the movement of diaphragm, which clearly shows the diaphragm motion patterns during different breathing modes.

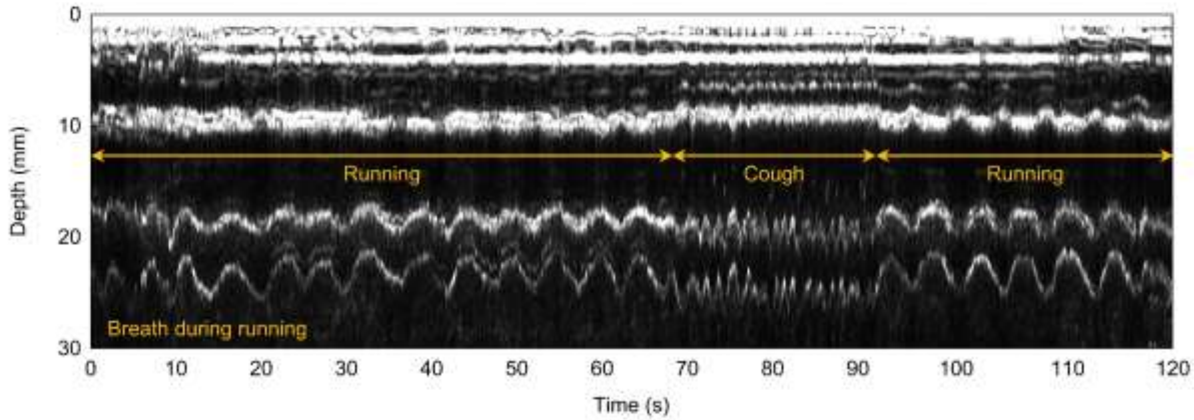

Supplementary Fig. 18 | Testing potential motion artefacts during running on a treadmill. We used the wearable ultrasound system to continuously record the diaphragm signals when a participant ran on a treadmill to test if the exercise could introduce motion artefacts. At the beginning, the participant had stable running and breathing. The ultrasound M-mode image showed that regular running did not cause obvious motion artifacts or affect the monitoring quality of diaphragm. Then the subject consciously coughed to introduce strong diaphragm movements. Although the diaphragm signal showed unstable motions, this was intrinsically because coughing actively caused the relative motions between the ultrasound device and the diaphragm. After coughing, the ultrasound signals became stable again with clearly distinguishable inspiration and expiration patterns. In conclusion, because our wearable ultrasound device could be stably attached to the skin, daily activity and regular excise do not introduce obvious artifacts.

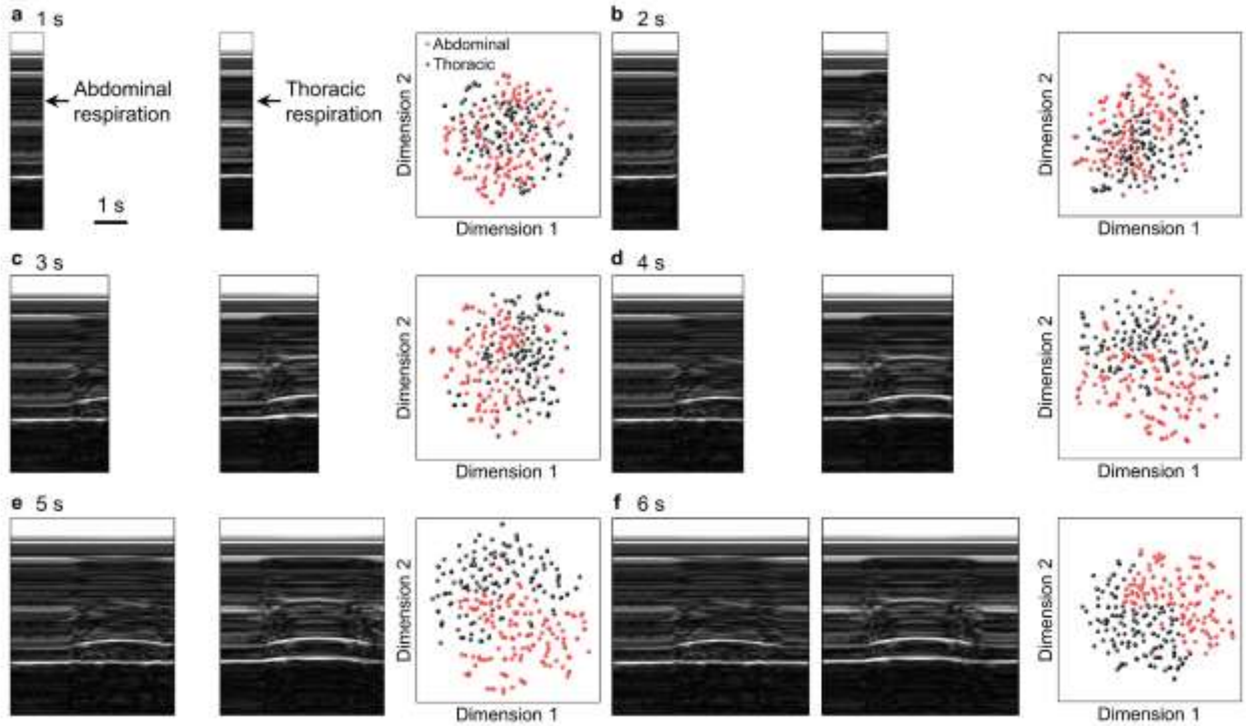

Supplementary Fig. 19 | *t*-SNE plots of M-mode images under different respiration modes. Abdominal respiration contracts the diaphragm and is deep. The belly expands during this type of respiration to make sure diaphragm has the space to contract. Thoracic respiration does not involve the diaphragm and is shallow, during which the intercostal muscles draw a minimal volume of air into the chest. **a-f**, M-mode images corresponding to abdominal respiration and thoracic respiration with different durations. When the duration is short, the two respiration modes may have similar M-mode images. So, they are not clearly separated. As the duration increases, the points corresponding to the two different respiration modes in the *t*-SNE plots are more clearly separated. The larger the separation between these points, the greater the differences in the corresponding data.

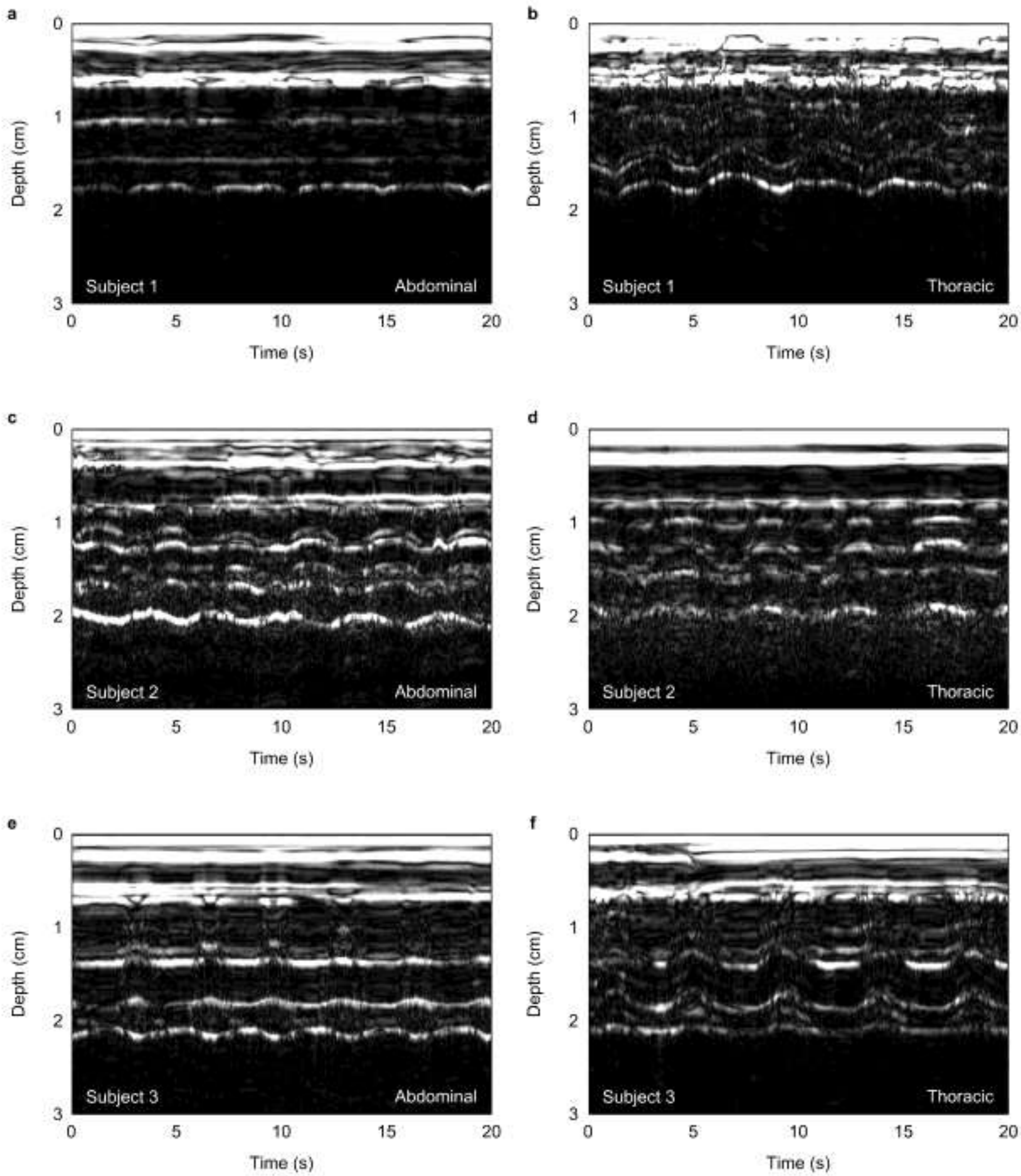

Supplementary Fig. 20 | M-mode images of subjects 1, 2, and 3 during abdominal and thoracic respirations. The diaphragm shows large thickening fractions for all participants in the (**a**), (**c**), and (**e**) abdominal breathing mode, but small thickening degrees in the (**b**), (**d**), and (**f**) thoracic breathing modes.

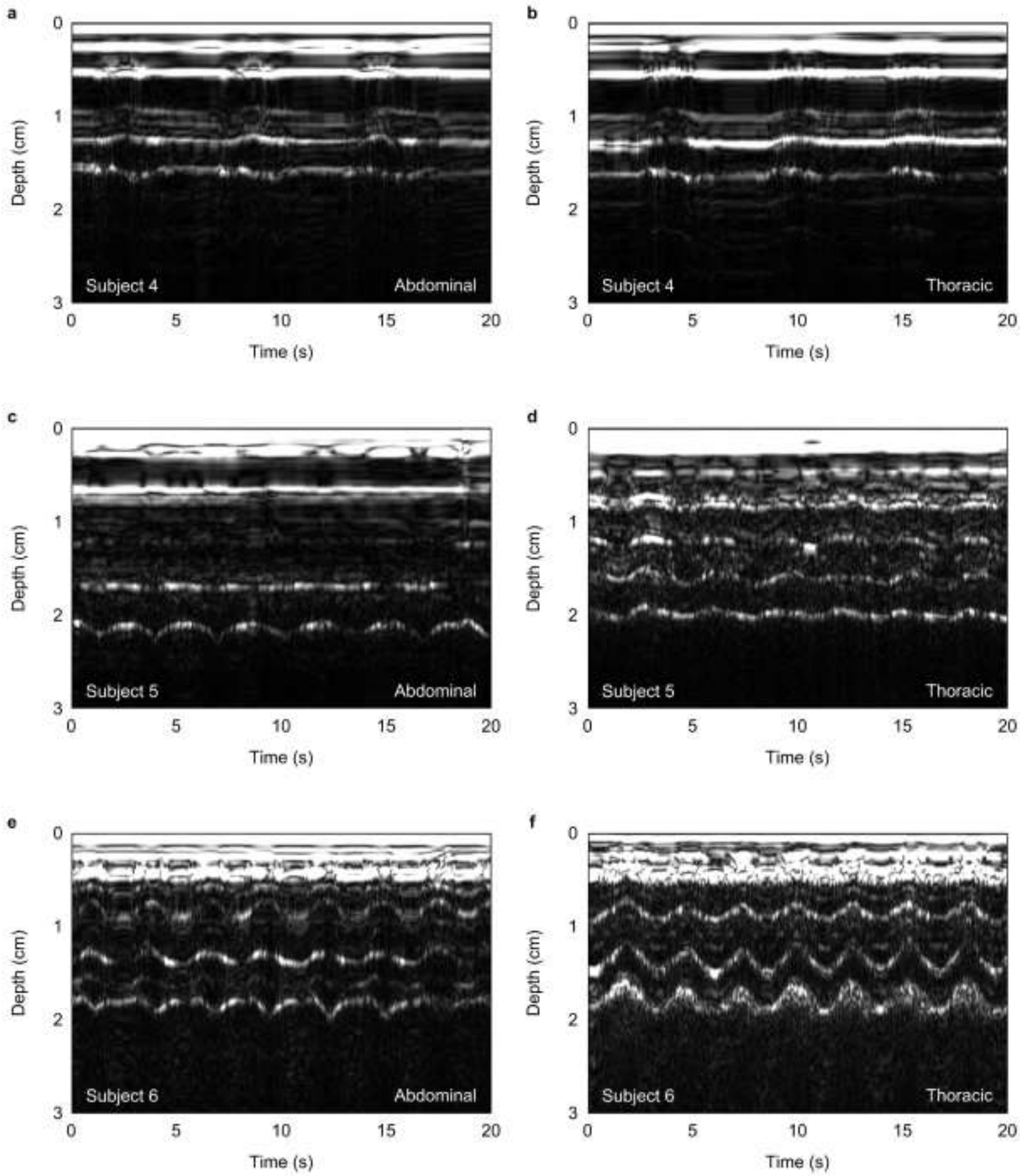

Supplementary Fig. 21 | M-mode images of subjects 4, 5, and 6 during abdominal and thoracic respirations. The diaphragm shows large thickening fractions for all participants in the (**a**), (**c**), and (**e**) abdominal breathing mode, but small thickening degrees in the (**b**), (**d**), and (**f**) thoracic breathing modes.

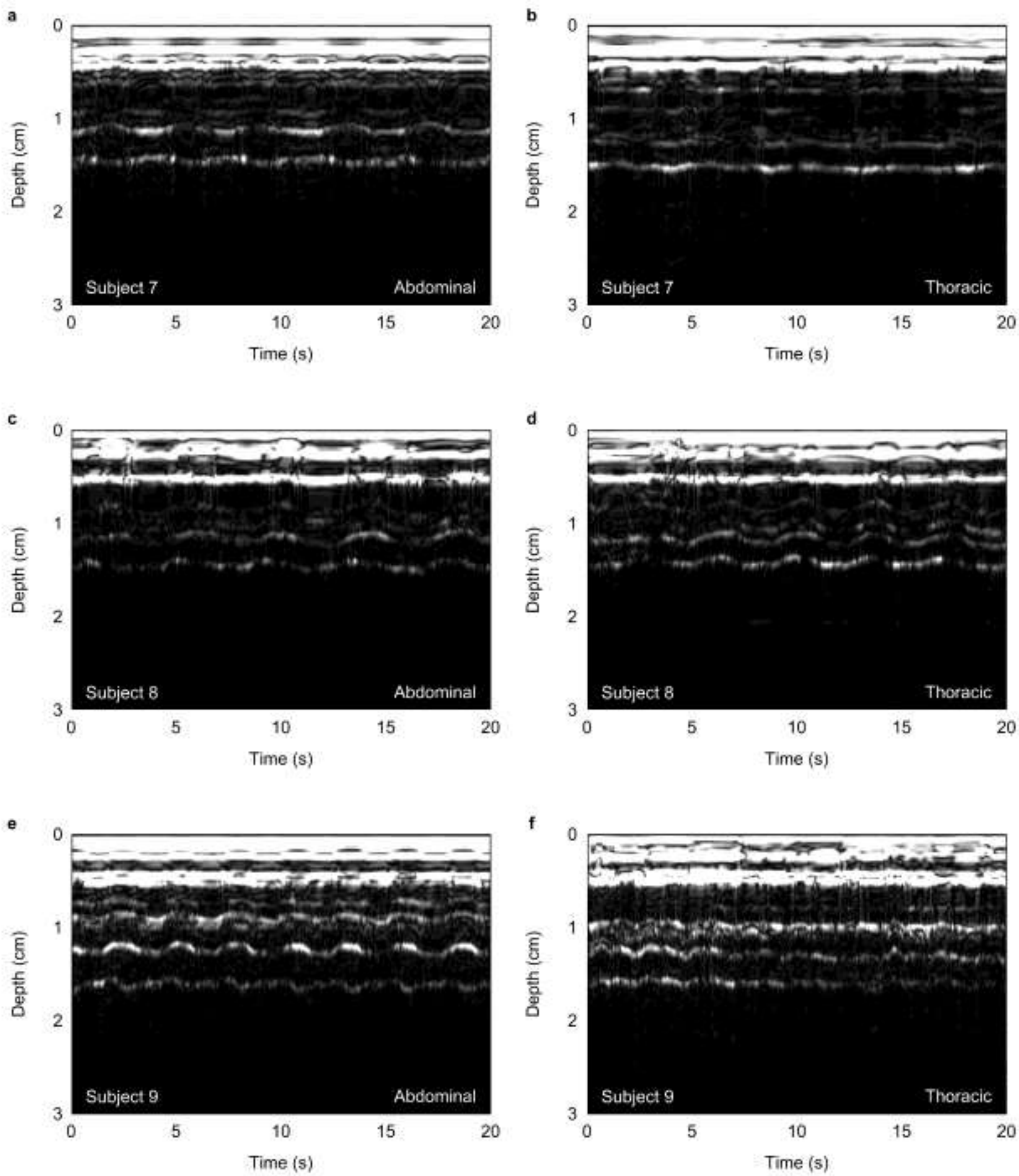

Supplementary Fig. 22 | M-mode images of subjects 7, 8, and 9 during abdominal and thoracic respirations. The diaphragm shows large thickening fractions for all participants in the (**a**), (**c**), and (**e**) abdominal breathing mode, but small thickening degrees in the (**b**), (**d**), and (**f**) thoracic breathing modes.

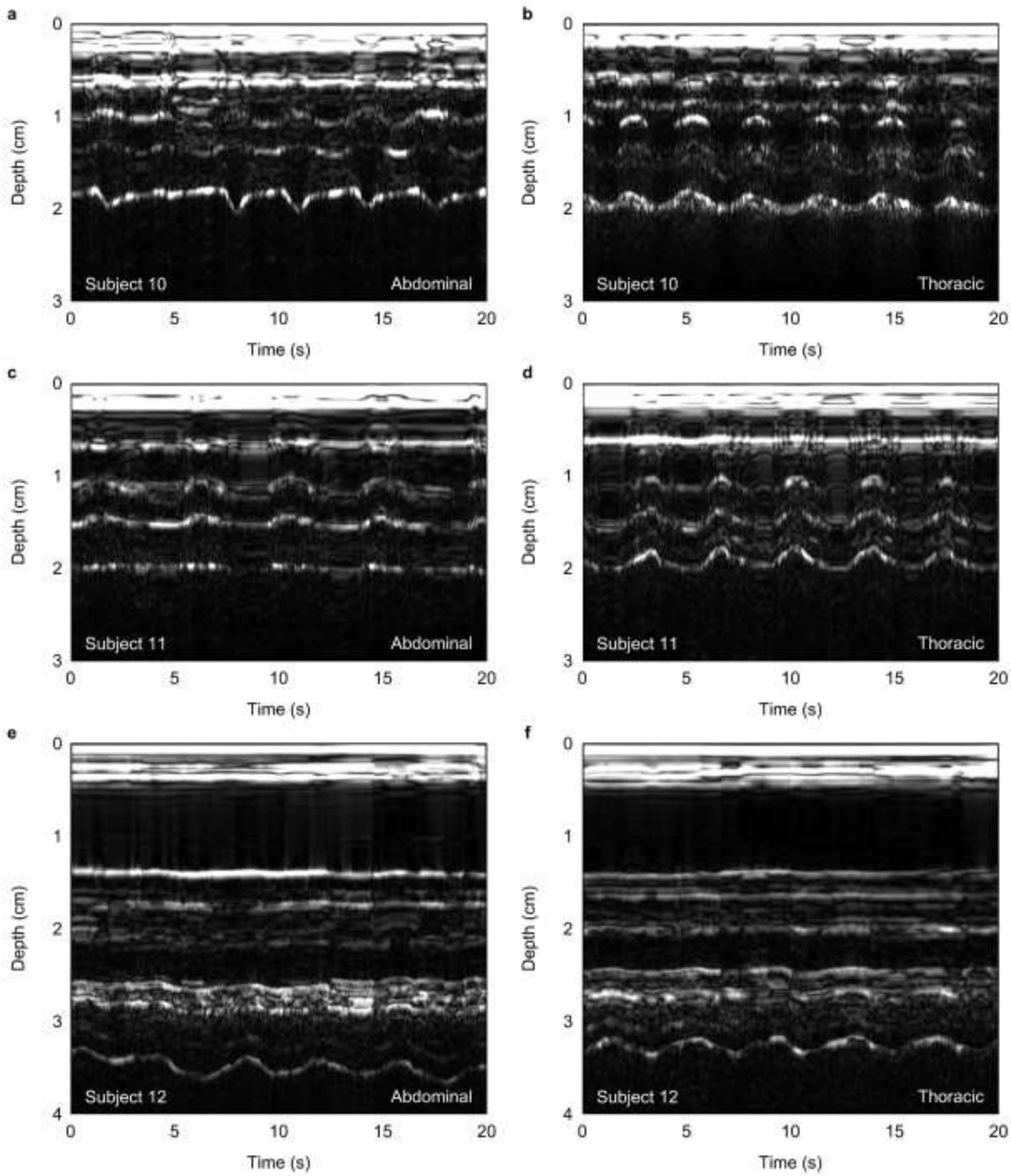

Supplementary Fig. 23 | M-mode images of subjects 10, 11, and 12 during abdominal and thoracic respirations. The diaphragm shows large thickening fractions for all participants in the (**a**), (**c**), and (**e**) abdominal breathing mode, but small thickening degrees in the (**b**), (**d**), and (**f**) thoracic breathing modes.

a

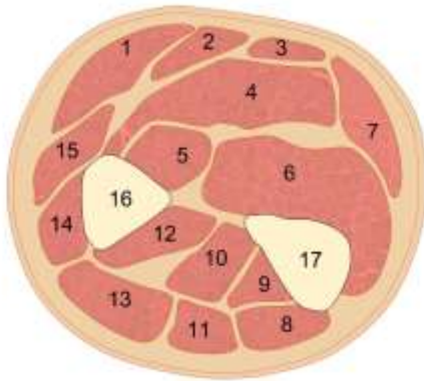

b

Muscle number	Muscle	Related joints
1	Brachioradialis muscle	Elbow
2	Flexor carpi radialis muscle	Wrist
3	Palmaris longus muscle	Wrist
4	Flexor digitorum superficialis muscle	Index, middle, ring, and little fingers
5	Flexor pollicis longus muscle	Thumb
6	Flexor digitorum profundus muscle	Index, middle, ring, and little fingers
7	Flexor carpi ulnaris muscle	Wrist
8	Extensor carpi ulnaris muscle	Wrist
9	Extensor pollicis longus muscle	Thumb
10	Extensor pollicis brevis muscle	Thumb
11	Extensor digiti minimi muscle	Little finger
12	Abductor pollicis longus muscle	Thumb
13	Extensor digitorum muscle	Index, middle, ring and little fingers
14	Extensor carpi radialis brevis muscle	Wrist
15	Extensor carpi radialis longus muscle	Wrist

Supplementary Fig. 24 | Components of the forearm muscles. a, Cross sectional schematics showing the typical spatial distribution of the muscles in the forearm[67]. **b**, Correlations between the muscles and fingers and wrist in typical subjects. 16 and 17 are radius and ulna bones, respectively.

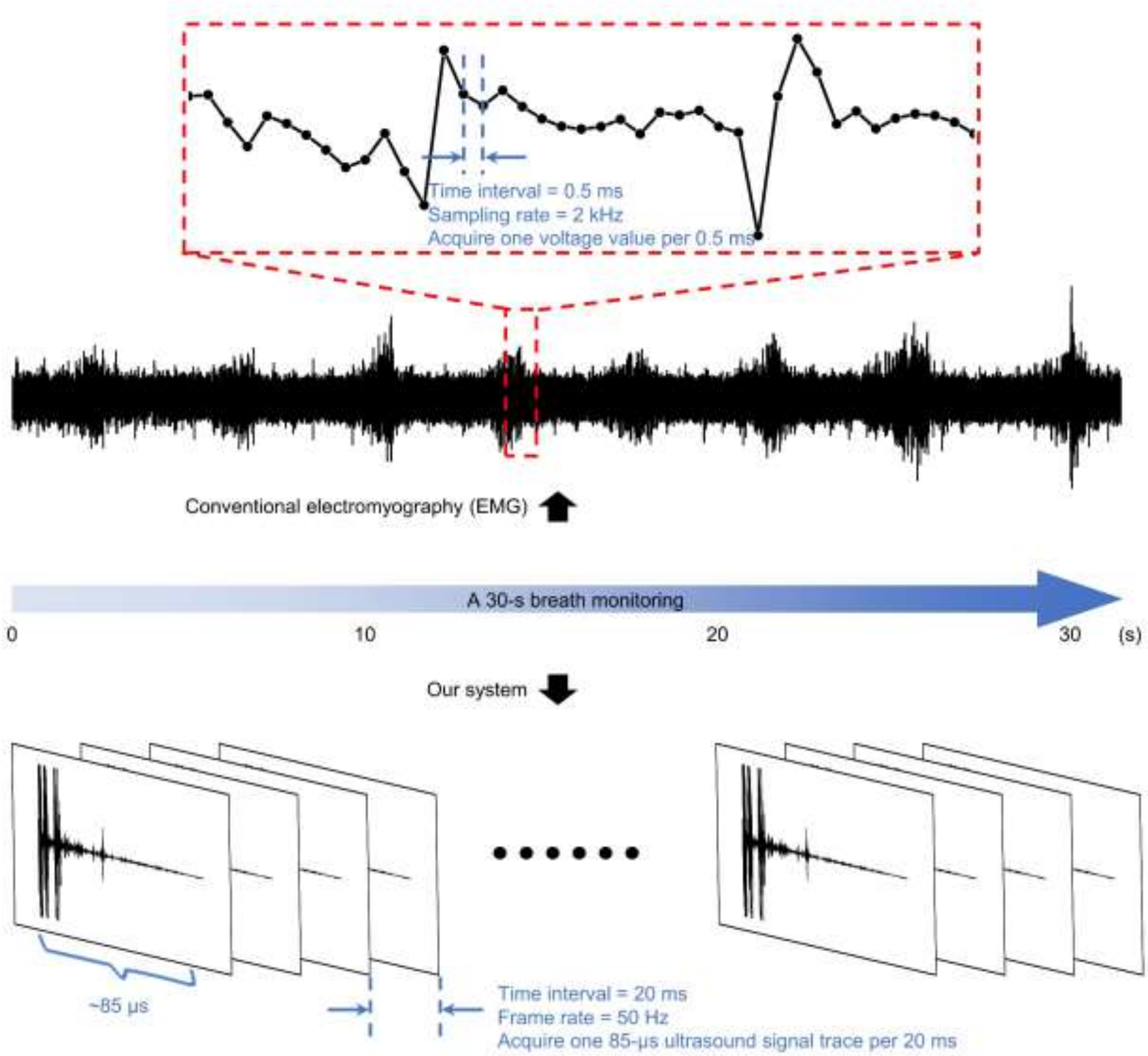

Supplementary Fig. 25 | Comparison of data acquisition and temporal resolution between conventional electromyography and the ultrasound system in this work. We performed 30-s breath monitoring as an example. In conventional electromyography, the surface electrodes measure one voltage value from the skin surface every 0.5 ms. In this case, its temporal resolution is 2 kHz. Our ultrasound system acquires one ultrasound signal trace every 20 ms (corresponding to a temporal resolution of 50 Hz), while each signal trace lasts 85 µs containing 1024 data points. This ultrasound signal trace represents the propagation and reflection of ultrasound waves from the skin to deep tissue (~6.6 cm in depth), which contains the spatial information of deep tissue. To summarize, our ultrasound system has a lower temporal resolution (i.e., 50 Hz) lower than the conventional electromyography (2 kHz), but it contains much more spatial information of muscles for every data acquisition. The applications scenarios of the EMG system and our ultrasound system could be based on their different advantages. The EMG system could be constructed by simple circuits, and capture the mixed signals from a large volume of muscles with several electrodes. Therefore, the EMG system is very suitable for activity or abnormality monitoring of a large area. As a comparison, our ultrasound system can image the detailed movements of deep muscles with a submillimeter resolution, which allows it to accurately monitor detailed muscle motion activities. The temporal resolution limit of our ultrasound system is intrinsically decided by the propagation time of ultrasound waves. Because the transceiving process requires the ultrasound wave to complete the round-trip propagation in the tissue, the minimum time consumption for each frame of data acquisition, which determines the temporal resolution limit of our system, can be calculated as $2D/c$, where D is the detection depth, and c is the speed of sound in tissues. Assuming the sensing depth is about 6.6 cm, as demonstrated in this work, the signal acquisition time will be ~85 μs because the sound speed is ~1540 m/s in muscle. Then, 85 μs will be the temporal resolution limit, which corresponds to the frame rate limit of ~11.7 kHz of our wearable ultrasound system.

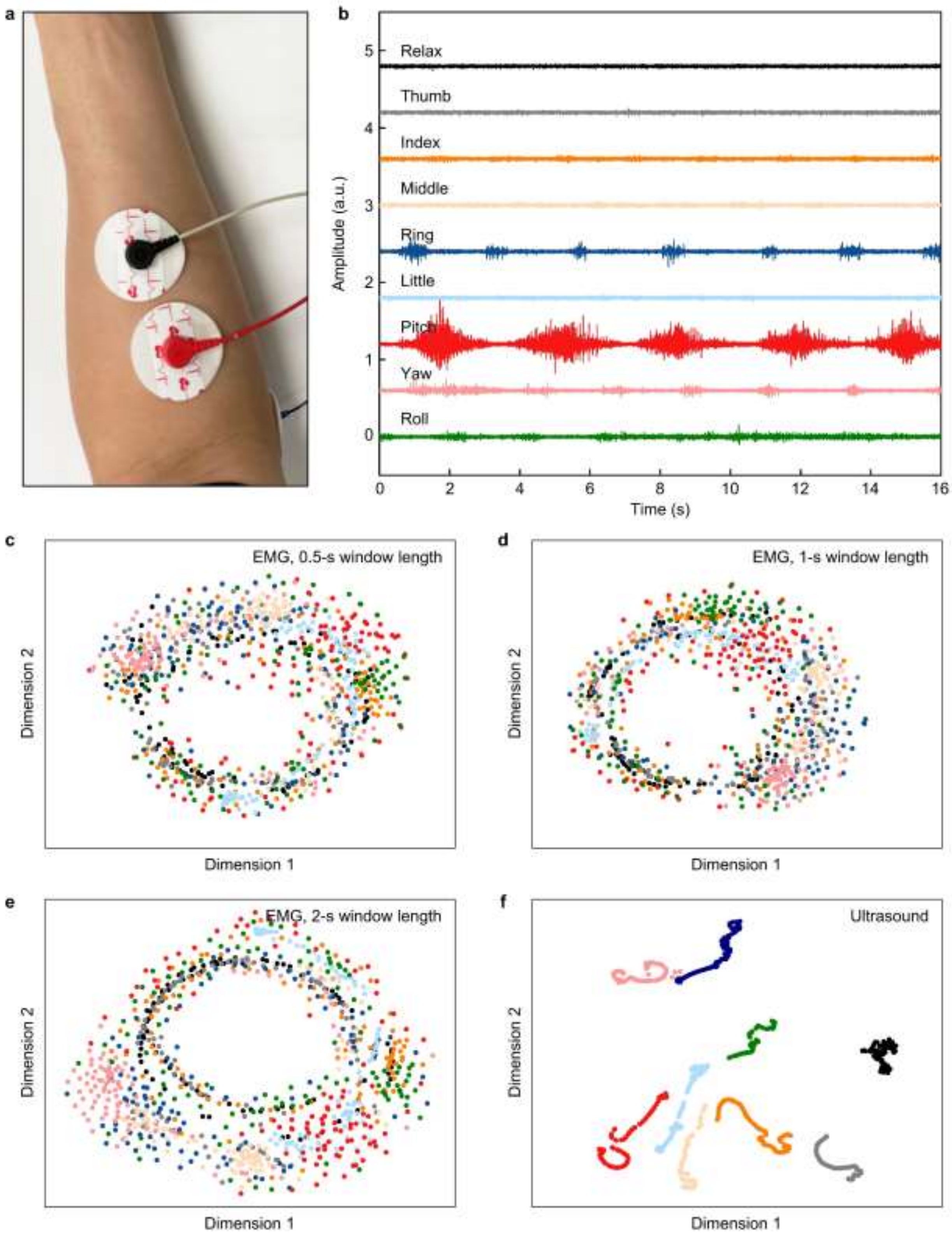

Supplementary Fig. 26 | Surface EMG is insensitive to normal finger and wrist motions. a, Image of electrode placement for surface EMG measurements in this work. **b**, Single-channel surface EMG signals during relaxation, gently bending five fingers, and rotating wrist along pitch, yaw, and roll axes. Raw surface EMG signals were filtered by a 60 Hz notch filter and a 20~500 Hz bandpass filter because surface EMG signals are mainly in this frequency band [66]. The single-channel surface EMG signals during finger bending have low signal to noise ratio and low sensitivity to finger motion. Signals of wrist pitching are relatively strong. But the other two motions of the wrist, yawing and rolling, have low signal amplitudes. **c-e**, *t*-SNE plots of single-channel surface EMG signals corresponding to different segmentation lengths. The scatter points share the same color codes as the signals in **b**. We randomly selected 100 segments from a continuous 1 min surface EMG signal for each kind of motion. The fingers/wrist repeatedly did the bending/rotation every ~2 s within the 1 min measurement. The duration of each segment was set as 0.5 s, 1 s, or 2 s. Such segment window lengths are typical for surface EMG applications[66]. **f**, *t*-SNE plot of EcMG signals corresponding to hand motions like those in Fig. 4B and fig. S23. These *t*-SNE plots show that points of different motions are mixed for surface EMG signals, which means the surface EMG signals of different hand motions have small differences. It is challenging for single-channel surface EMG signals to accurately distinguish different hand gestures. However, the points of different motions are perfectly separated for single-channel EcMG signals, which means ultrasound signals have high differentiation accuracies for different hand gestures. Therefore, EcMG signals are more sensitive to normal muscle contraction than surface EMG signals.

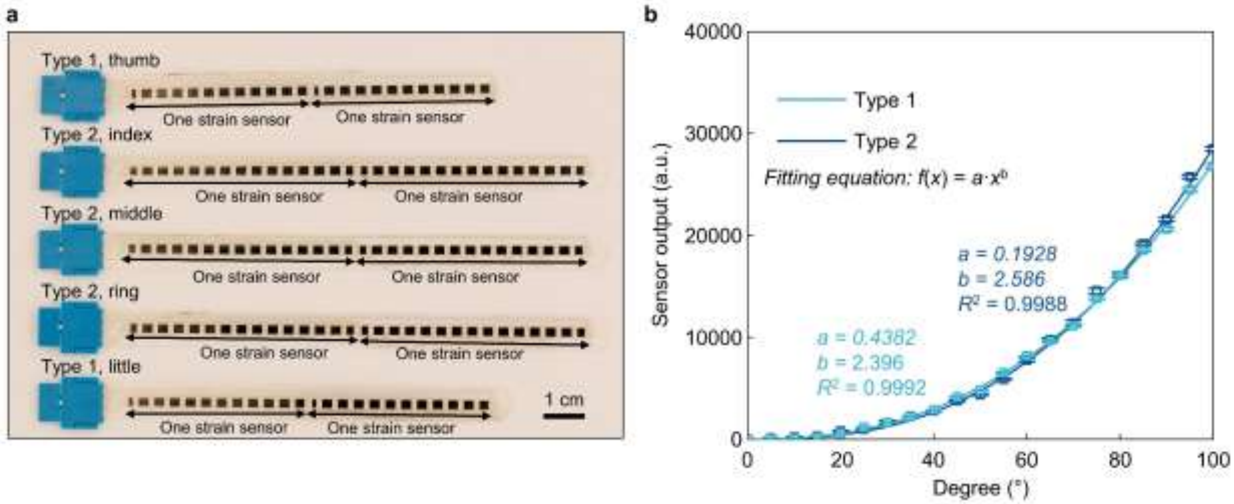

Supplementary Fig. 27 | Calibration of strain sensors. a, Image of the strain sensors used for measuring finger joint angles. Each sensor contains two sub strain sensors for two joints measurement. Two sensors of type 1 are used to measure the two joints of the thumb and the little fingers. Three sensors of type 2 are used to measure two joints of the index, middle, and ring fingers. **b**, Calibration curves of the two types of sensors show the relationships between the bending angle and sensor output. The sub sensors of the same type are exactly the same.

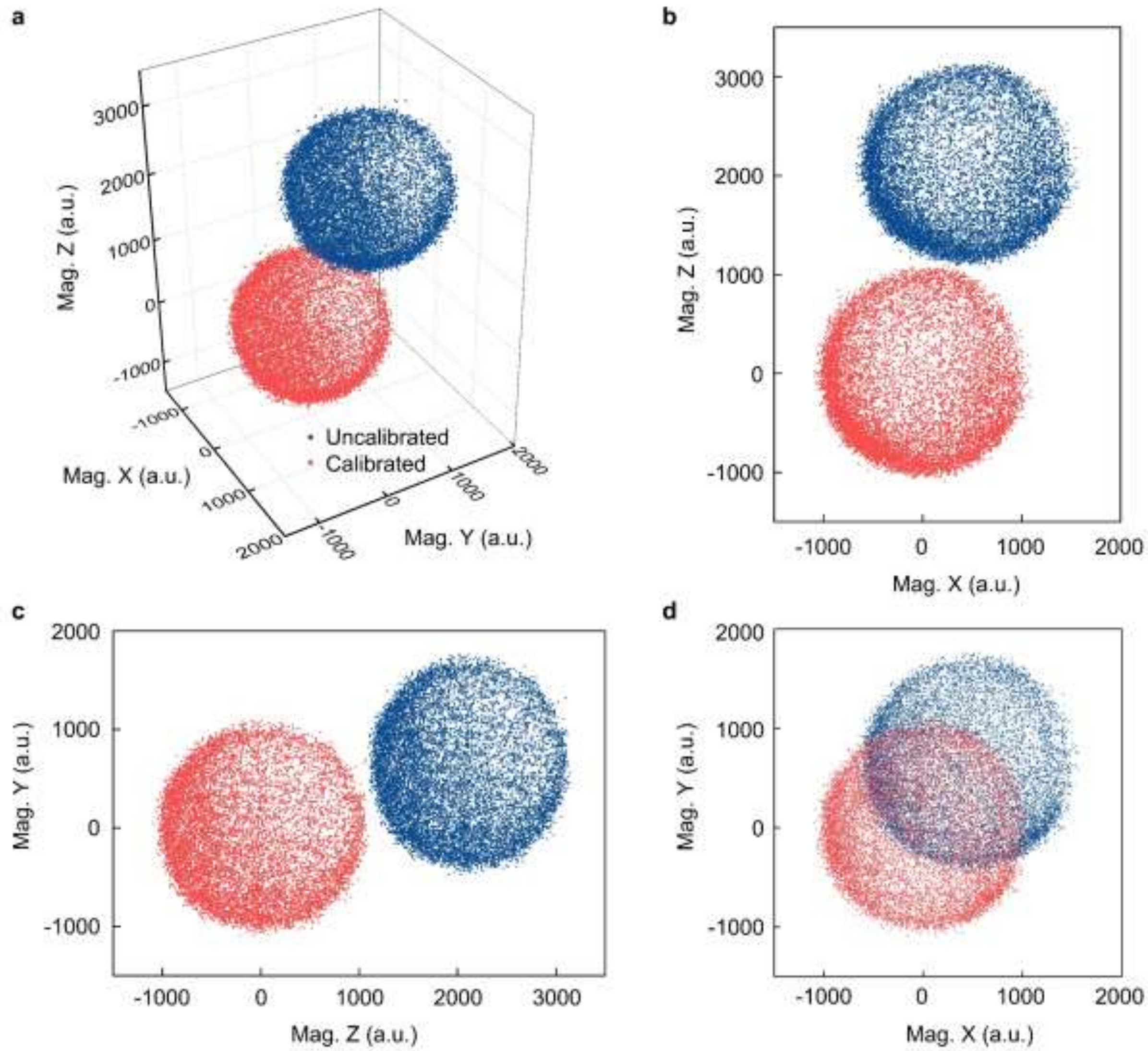

Supplementary Fig. 28 | Calibration of the magnetometer outputs. a, The blue dots are the raw magnetometer output without compensating for environmental distortion. The center of the dot cloud is shifted away from the origin of the coordinate system. The red dots are the calibrated magnetometer data. The center of the red dot cloud is at the origin of the coordinate system. **b-d**, The projection of raw and calibrated data in X-Z, Y-Z, and X-Y planes, respectively.

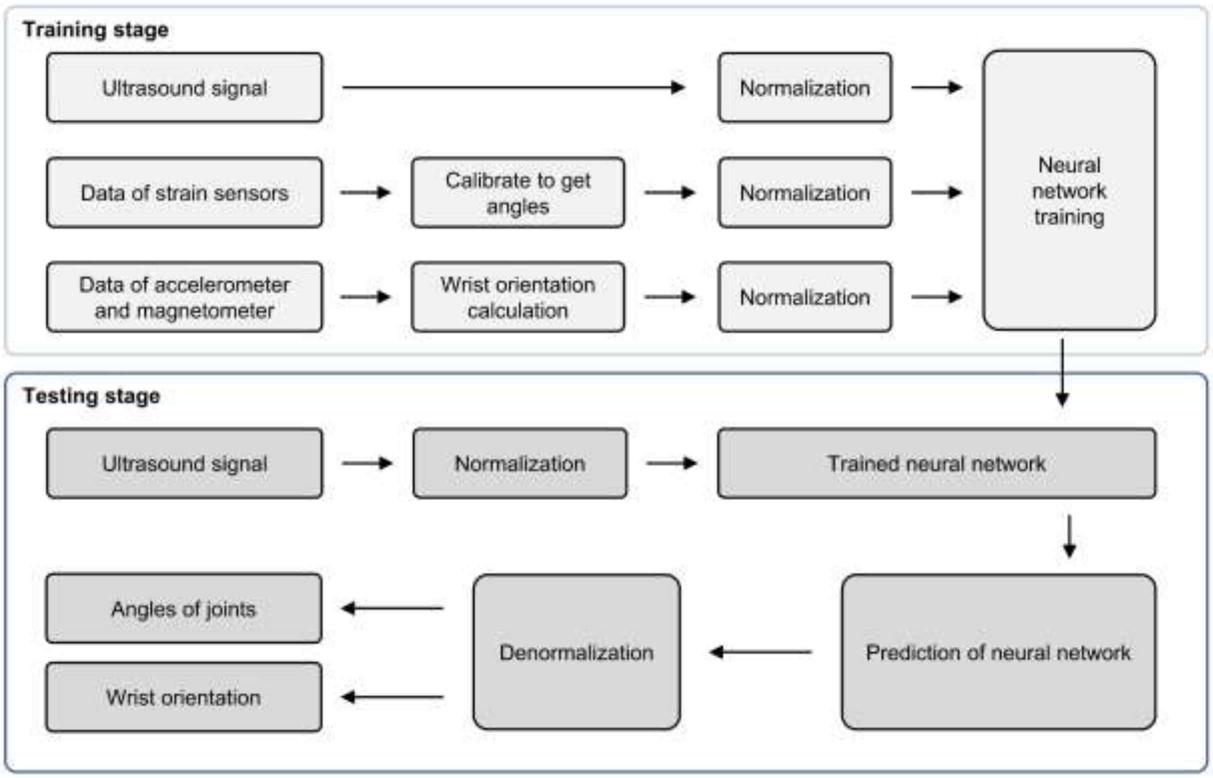

Supplementary Fig. 29 | Flowchart of training and testing of deep learning-based continuous hand gesture tracking. At the training stage, we need to collect the training dataset, which contains paired ultrasound signals and the hand gesture data. The hand gesture data is composed of bending angles of the fingers' joints and rotation angles of the wrist, which are measured by strain sensors and a six-axis IMU sensor (three-axis accelerometer, three-axis magnetometer), respectively. Calibration is required to transform the strain sensor output to bending angle. The ultrasound signals, bending angles of the finger joints, and rotation angles of the wrist are all normalized before being fed into the neural network for training. After the neural network is trained, it can be applied for real-time hand gesture tracking. At the testing stage, the ultrasound signal is also normalized before fed into the trained neural network. The outputs of the neural network are denormalized to acquire the finger joint bending and wrist rotation angles.

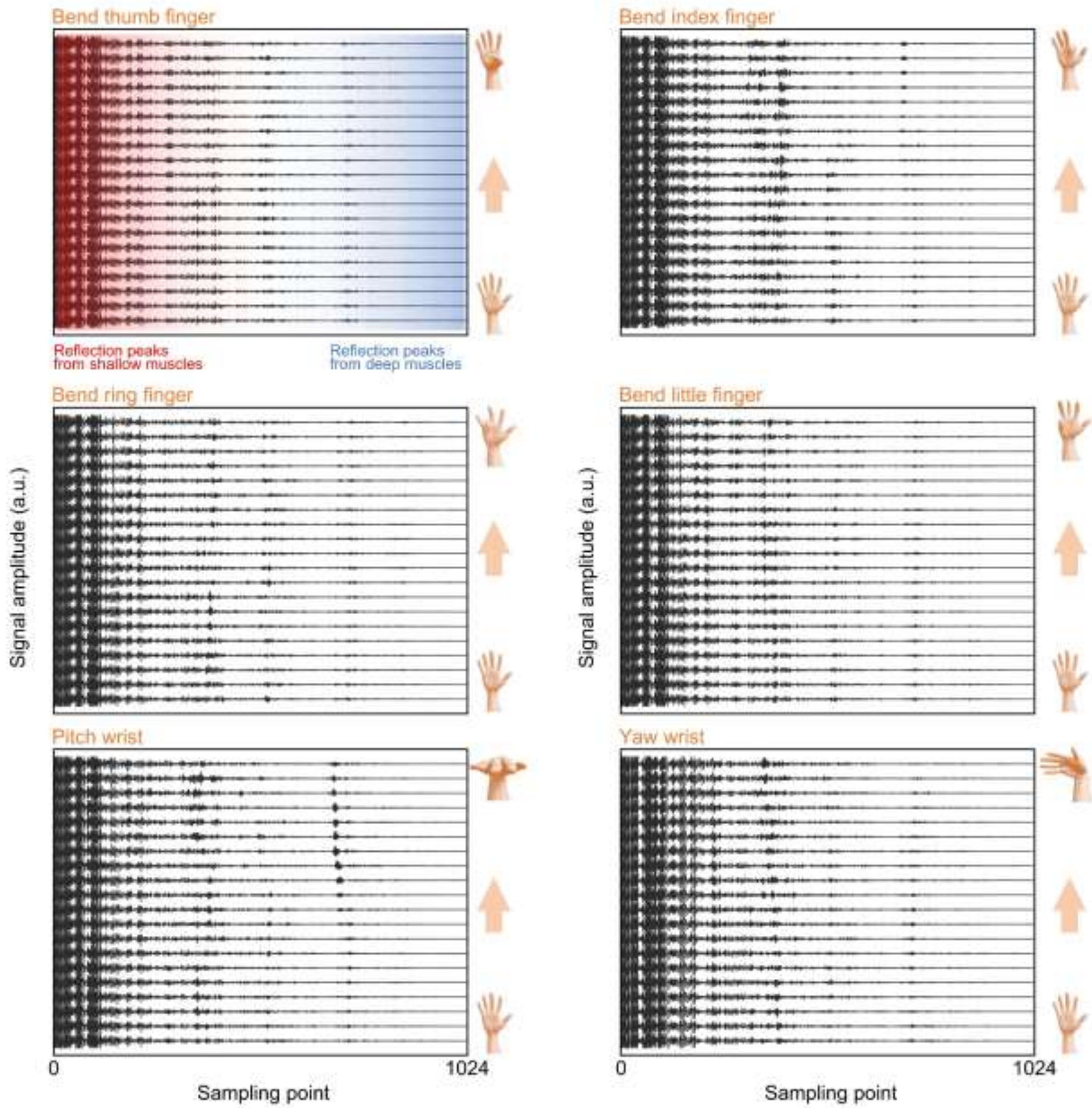

Supplementary Fig. 30 | RF signals as the fingers bend and the wrist rotates. Each panel shows 20 RF signals overlapped to illustrate the evolvement of echo peaks as the fingers and wrist move. The single transducer for hand gesture tracking has a wide beam. One RF data contains signals from all muscles in such a wide beam. Different muscles at the same radial depth appear at the same time in the RF signal. The peak shifts only reflect motion of muscles in the radial direction. Therefore, it is not possible to quantify the absolute motion of a specific muscle just based on the shifted peak.

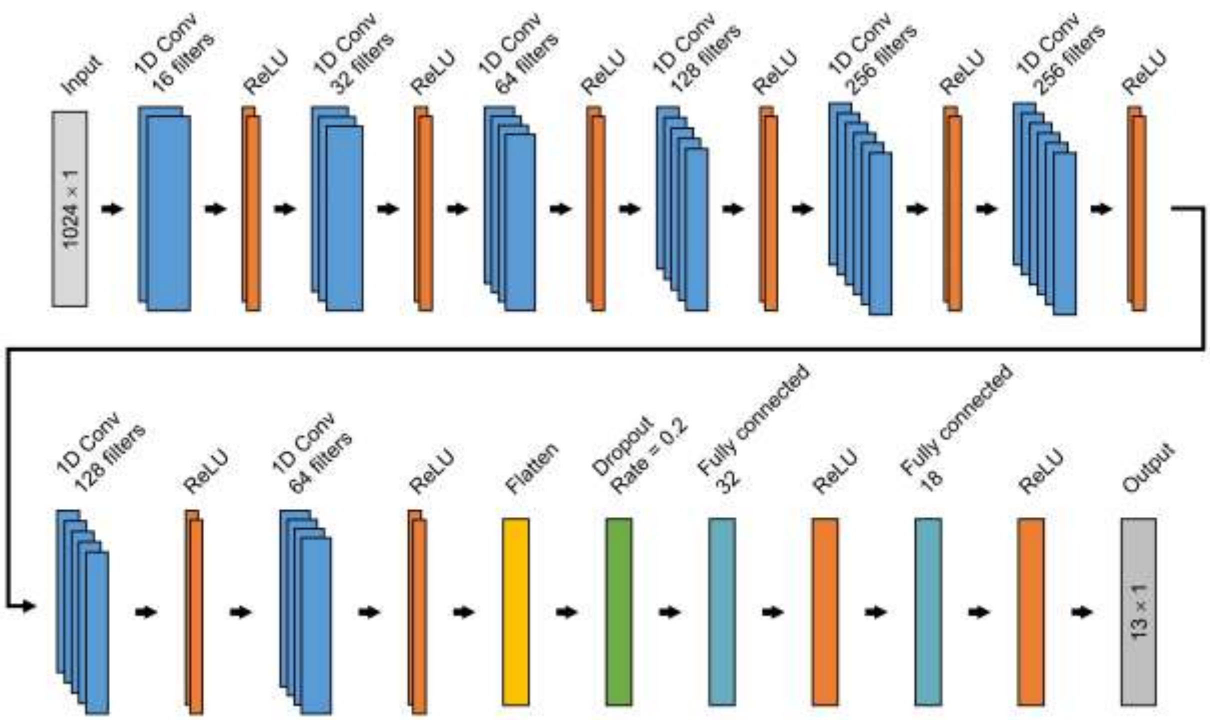

Supplementary Fig. 31 | Framework of the deep neural network for hand gesture tracking. Although the muscle distribution decides the hand gesture and the RF signals, it is almost impossible to establish a mathematical relationship between the RF signals and the hand gesture. Therefore, we developed a deep neural network to infer the hand gesture from the RF signals. The input data are normalized RF signals, while the output layer has 13 numbers corresponding to 13 degrees of freedom of the hand gesture. Convolutional layers are well-suited to detect local patterns and structures in the data. In this work, the RF signal is 1D waveform. We first stack several 1D convolutional layers at the beginning and then adopt fully connected layers at the end of the network, which are typically used as the final layer for classification.

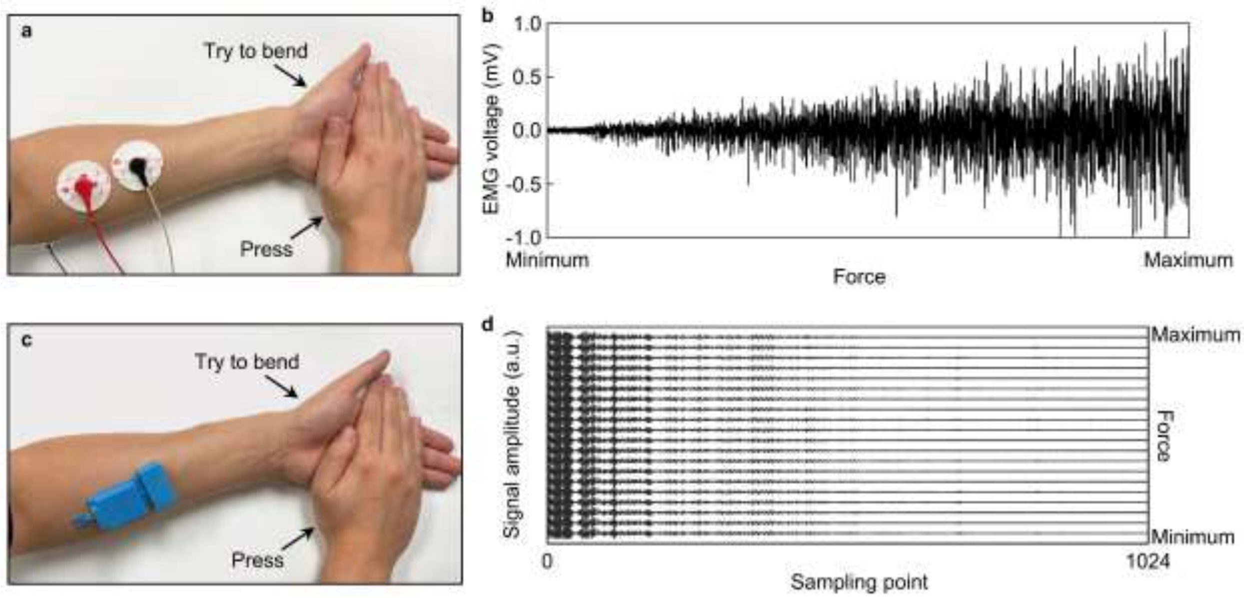

Supplementary Fig. 32 | Comparison between EMG and EcMG when the hand was constrained. a, Image of EMG measurement. **b**, EMG measures the biopotential in the muscle fibers. Therefore, even though the hand cannot move, the muscle fibers are still generating biopotentials, which can be captured by EMG electrodes. **c**, Image of EcMG measurement. **d**, Hand gesture is directly related to the spatial distribution of muscle fibers, which decides the ultrasound RF signals. Therefore, if the hand is constrained without moving, the RF signals show minimal changes even if the muscle force increases. In summary, EcMG directly measures the hand gesture by capturing the spatial distribution of muscle fibers[68], while EMG directly measures the force generated by muscle fibers[69].

Number of piezoelectric elements	Fully integrated wireless	Applications	Deep learning powered	Reference
256	No	Deep tissue elastography	No	[70]
144	No	Deep tissue hemodynamics	No	[31]
88	No	Heart imaging	Yes	[70]
32	Yes	Blood pressure monitoring	Yes	[71]
20	No	Blood pressure monitoring	No	[30]
1	Yes	Diaphragm monitoring and human-machine interface	Yes	**This work**

Supplementary Table 1 | Comparison between the device in this study and our previously reported works. The uniqueness of this device can be summarized in terms of transducer array design, system integration level, applications, and deep learning algorithm.

Component	Manufacture product number	Voltage range (V)	Regulator (if used)
Operational amplifier	ADA4895-1ARJZ-R7	3 ~ 10	N/A
Operational amplifier	ADA4897-1ARJZ-RL	3 ~ 10	N/A
Microcontroller	ATMEGA328P-ANR	2.7 ~ 5.5	MIC5205-3.3YM5-TR
ADC	PIC32MZ1024EFH064-I/MR	2.1 ~ 3.6	MIC5205-3.3YM5-TR
Wi-Fi module	ESP32-S3-WROOM-1	3.0 ~ 3.6	AMS1117

Supplementary Table 2 | Specifics of key components in the PCB. The power consumption of these chips is manageable by a commercial lithium-polymer battery.

Device/skin interface	Sensing area	Detection mode	Health monitoring	Human-machine interface	Deep learning powered	Reference
Rigid	Deep tissue	Continuous doppler	Carotid artery blood flow	No	No	[39]
Rigid	Deep tissue	A-mode	Bladder volume	No	No	[40]
Rigid	Deep tissue	A-mode	Bladder volume	No	No	[41]
Soft	Skin surface	A-mode	Lung volume	No	No	[42]
Soft	Deep tissue	A-mode	Diaphragm movement	Yes	Yes	**This work**

Supplementary Table 3 | Comparison with other fully integrated wearable ultrasound devices. The device in this work has soft interface with the skin, ensuring stable adhesion and acoustic coupling between the single transducer and the skin. Additionally, the device in this work is powered by a deep learning algorithm, which enables continuous tracking of hand gestures for human-machine interface.

Transducer type	Transducer size	Channel number	Sensing mode	Wearable circuit	Use cases	Reference
Rigid linear probe	~38 mm in width	128	B-mode image	No	Classify 15 discrete hand gestures	72
Rigid linear probe	~38 mm in width	N/A	B-mode image	No	Classify 6 discrete hand gestures	73
Rigid phase array	>19.2 mm in width	1	Radiofrequency signal	No	Classify 9 discrete hand gestures	74
Soft single transducers	20 mm × 20 mm × 0.28 mm	3	Radiofrequency signal	No	Classify 5 discrete hand gestures	75
Rigid single transducers	Ø 9 mm × 11 mm	8	Radiofrequency signal	No	Classify 8 discrete hand gestures; Track continuous wrist rotation	76
Rigid single transducers	16 mm in diameter	8	Radiofrequency signal	No	Classify 11 discrete hand gestures or 9 discrete facial gestures; Track continuous thumb angle or the angle of all other four fingers	77
Soft transducer array	15 mm × 15 mm × 3 mm; 100 mm × 100 mm × 3 mm	16	Radiofrequency signal	No	Track continuous arm rotation angle	78
Soft single transducer	6 mm × 6 mm × 1.2 mm	1	Radiofrequency signal	Yes	Track 13 continuous angles of the hand joints	**This work**

Supplementary Table 4 | Comparison among different EcMG studies for hand gesture recognition. We developed a fully wearable device, including a soft transducer and a compact controlling circuit, eliminating the tethering wires to bulky equipment. Soft transducers enable reliable contact with the skin, ensuring stable acoustic coupling.

Method	Data	Discrete/ Continuous	Kinds of motions	Accuracy of classification	Number of angles	Error of angles	Citation
EMG	4-ch EMG signal	Discrete	3	95.4%	-	-	[79]
	4-ch EMG signal	Discrete	6	91.1%	-	-	[80]
	5-ch EMG signal	Discrete	10	92.75%	-	-	[81]
	6-ch EMG signal	Discrete	15	98%	-	-	[82]
	8-ch EMG signal	Discrete	6	95.3%	-	-	[83]
	8-ch EMG signal	Discrete	6	90.85%	-	-	[84]
	48-ch EMG signal	Discrete	9	95.8%	-	-	[85]
	57-ch EMG signal	Discrete	7	~98%	-	-	[86]
	192-ch EMG signal	Discrete	11	96.5%	-	-	[87]
	8-ch EMG signal	Discrete/ Continuous	7	95.64%	2	Linear regression $R^2 = 0.843$	[88]
	8-ch EMG signal	Discrete/ Continuous	-	-	21	Median error of 6.4°, 90%-ile error 18.3°	[52]
	96-ch EMG signal	Discrete/ Continuous	-	-	5	>10°	[89]
EcMG	3-ch RF signal	Discrete	5	92.5 ± 7.6%	-	-	[75]
	8-ch RF signal	Discrete/ Continuous	8	96.5 ± 1.7%	1	linear regression $R^2 = 0.954 \pm 0.012$	[76]
	8-ch RF signal	Discrete/ Continuous	11	93.4%	2	1.7° for thumb and 6.5° for other four fingers	[77]
	B-mode image	Discrete	6	94%	-	-	[73]
	B-mode image	Discrete	15	91%	-	-	[72]
	16-ch RF signal	Discrete	1	-	-	-	[78]
	1-ch RF signal	Discrete	9	67.01%	-	-	[74]
	1-ch RF signal	**Continuous**	**-**	**-**	**13**	**7.9°**	**This work**

Supplementary Table 5 | Accuracies of hand gesture recognition based on EMG and EcMG. Previous studies only achieved classifying specific discrete hand gestures, or tracking a few hand joints using multiple-channel signals. In this work, we demonstrated continuous tracking of angles of 13 hand joints using one-channel signal. We used strain and IMU sensors to acquire the finger bending angles and the wrist rotation angles as the ground truth of hand gesture. Then, we developed a deep neural network to relate the RF signals to the angles of the fingers and wrist.

Supplementary Video 1: Simultaneous measurements of EcMG and EMG signals as fingers bend and wrist rotates.

Supplementary Video 2: Real-time virtual bird control by correlating the pitch angle of wrist with the height of the virtual bird.

Supplementary Video 3: Real-time robotic arm control by correlating the pitch angle of wrist and finger joint angle with motions of robotic arm.

References

1 Chung, H. U. *et al.* Skin-interfaced biosensors for advanced wireless physiological monitoring in neonatal and pediatric intensive-care units. *Nature Medicine* **26**, 418-429 (2020).

2 Jeong, H. *et al.* Differential cardiopulmonary monitoring system for artifact-canceled physiological tracking of athletes, workers, and COVID-19 patients. *Science Advances* **7**, eabg3092 (2021).

3 Tan, C. *et al.* A high performance wearable strain sensor with advanced thermal management for motion monitoring. *Nature Communications* **11**, 1-10 (2020).

4 Kwak, J. W. *et al.* Wireless sensors for continuous, multimodal measurements at the skin interface with lower limb prostheses. *Science Translational Medicine* **12**, eabc4327 (2020).

5 Schwartz, G. *et al.* Flexible polymer transistors with high pressure sensitivity for application in electronic skin and health monitoring. *Nature Communications* **4**, 1-8 (2013).

6 Yu, Y. *et al.* Biofuel-powered soft electronic skin with multiplexed and wireless sensing for human-machine interfaces. *Science Robotics* **5**, eaaz7946 (2020).

7 Baker, L. B. *et al.* Skin-interfaced microfluidic system with personalized sweating rate and sweat chloride analytics for sports science applications. *Science Advances* **6**, eabe3929 (2020).

8 Moin, A. *et al.* A wearable biosensing system with in-sensor adaptive machine learning for hand gesture recognition. *Nature Electronics* **4**, 54-63 (2021).

9 Taccola, G. *et al.* Using EMG to deliver lumbar dynamic electrical stimulation to facilitate cortico-spinal excitability. *Brain Stimulation* **13**, 20-34 (2020).

10 Bellani, G. *et al.* Measurement of diaphragmatic electrical activity by surface electromyography in intubated subjects and its relationship with inspiratory effort. *Respiratory care* **63**, 1341-1349 (2018).

11 Kim, M. K. *et al.* Flexible submental sensor patch with remote monitoring controls for management of oropharyngeal swallowing disorders. *Science Advances* **5**, eaay3210 (2019).

12 Kim, T. *et al.* Ultrathin crystalline-silicon-based strain gauges with deep learning algorithms for silent speech interfaces. *Nature Communications* **13**, 5815 (2022).

13 Eskes, M. *et al.* Simulation of facial expressions using person-specific sEMG signals controlling a biomechanical face model. *International Journal of Computer Assisted Radiology and Surgery* **13**, 47-59 (2018).

14 Lee, K. *et al.* Mechano-acoustic sensing of physiological processes and body motions via a soft wireless device placed at the suprasternal notch. *Nature Biomedical Engineering* **4**, 148-158 (2020).

15 Chun, K. S. *et al.* A skin-conformable wireless sensor to objectively quantify symptoms of pruritus. *Science Advances* **7**, eabf9405 (2021).

16 Baek, S. *et al.* Spatiotemporal measurement of arterial pulse waves enabled by wearable active-matrix pressure sensor arrays. *ACS Nano* **16**, 368-377 (2021).

17 Wang, Y. *et al.* A durable nanomesh on-skin strain gauge for natural skin motion monitoring with minimum mechanical constraints. *Science Advances* **6**, eabb7043 (2020).

18 Araromi, O. A. *et al.* Ultra-sensitive and resilient compliant strain gauges for soft machines. *Nature* **587**, 219-224 (2020).

19 Ryu, D. *et al.* Comprehensive pregnancy monitoring with a network of wireless, soft, and flexible sensors in high-and low-resource health settings. *Proceedings of the National Academy of Sciences* **118**, e2100466118 (2021).

20 Rwei, A. Y. *et al.* A wireless, skin-interfaced biosensor for cerebral hemodynamic monitoring in pediatric care. *Proceedings of the National Academy of Sciences* **117**, 31674-31684 (2020).

21 Fortin, J. *et al.* A novel art of continuous noninvasive blood pressure measurement. *Nature Communications* **12**, 1387 (2021).

22 Gao, X. *et al.* A photoacoustic patch for three-dimensional imaging of hemoglobin and core temperature. *Nature Communications* **13**, 7757 (2022).

23 Koh, A. *et al.* A soft, wearable microfluidic device for the capture, storage, and colorimetric sensing of sweat. *Science Translational Medicine* **8**, 366ra165-366ra165 (2016).

24 Thennadil, S. N. *et al.* Comparison of glucose concentration in interstitial fluid, and capillary and venous blood during rapid changes in blood glucose levels. *Diabetes Technology & Therapeutics* **3**, 357-365 (2001).

25 Claver, J. B., Mirón, M. V. & Capitán-Vallvey, L. Disposable electrochemiluminescent biosensor for lactate determination in saliva. *Analyst* **134**, 1423-1432 (2009).

26 Baca, J. T., Finegold, D. N. & Asher, S. A. Tear glucose analysis for the noninvasive detection and monitoring of diabetes mellitus. *The Ocular Surface* **5**, 280-293 (2007).

27 Kim, J., Campbell, A. S., de Ávila, B. E.-F. & Wang, J. Wearable biosensors for healthcare monitoring. *Nature Biotechnology* **37**, 389-406 (2019).

28 Isaacson, D., Mueller, J., Newell, J. & Siltanen, S. Imaging cardiac activity by the D-bar method for electrical impedance tomography. *Physiological Measurement* **27**, S43 (2006).

29 Victorino, J. A. *et al.* Imbalances in regional lung ventilation: a validation study on electrical impedance tomography. *American Journal of Respiratory and Critical Care Medicine* **169**, 791-800 (2004).

30 Wang, C. *et al.* Monitoring of the central blood pressure waveform via a conformal ultrasonic device. *Nature Biomedical Engineering* **2**, 687-695 (2018).

31 Wang, C. *et al.* Continuous monitoring of deep-tissue haemodynamics with stretchable ultrasonic phased arrays. *Nature Biomedical Engineering* **5**, 749-758 (2021).

32 Wang, F. *et al.* Flexible Doppler ultrasound device for the monitoring of blood flow velocity. *Science Advances* **7**, eabi9283 (2021).

33 Hu, H. *et al.* A wearable cardiac ultrasound imager. *Nature* **613**, 667-675 (2023).

34 Hu, H. *et al.* Stretchable ultrasonic arrays for the three-dimensional mapping of the modulus of deep tissue. *Nature Biomedical Engineering* **7**, *1321–1334 (2023).*.

35 Staudenmann, D., Roeleveld, K., Stegeman, D. F. & Van Dieën, J. H. Methodological aspects of SEMG recordings for force estimation–a tutorial and review. *Journal of Electromyography and Kinesiology* **20**, 375-387 (2010).

36 Jamal, M. Z. Signal acquisition using surface EMG and circuit design considerations for robotic prosthesis. *Computational Intelligence in Electromyography Analysis-A Perspective on Current Applications and Future Challenges* **18**, 427-448 (2012).

37 Rampichini, S., Vieira, T. M., Castiglioni, P. & Merati, G. Complexity analysis of surface electromyography for assessing the myoelectric manifestation of muscle fatigue: A review. *Entropy* **22**, 529 (2020).

38 Winder, S. *Analog and digital filter design*. (Elsevier, 2002).

39 Kenny, J.-É. S. Functional hemodynamic monitoring with a wireless ultrasound patch. *Journal of Cardiothoracic and Vascular Anesthesia* **35**, 1509-1515 (2021).

40 Hofstetter, S. *et al.* Dfree ultrasonic sensor in supporting quality of life and patient satisfaction with bladder dysfunction. *International Journal of Urological Nursing*.

41 van Leuteren, P. G., Klijn, A. J., de Jong, T. P. & Dik, P. SENS-U: validation of a wearable ultrasonic bladder monitor in children during urodynamic studies. *Journal of Pediatric Urology* **14**, 569. e561-569. e566 (2018).

42 Chen, A. *et al.* Wireless wearable ultrasound sensor on a paper substrate to characterize respiratory behavior. *ACS Sensors* **4**, 944-952 (2019).

43 Huang, Z. *et al.* Three-dimensional integrated stretchable electronics. *Nature Electronics* **1**, 473-480 (2018).

44 Dewitte, K., Fierens, C., Stockl, D. & Thienpont, L. M. Application of the Bland–Altman plot for interpretation of method-comparison studies: a critical investigation of its practice. *Clinical Chemistry* **48**, 799-801 (2002).

45 Yu, J., Qin, M. & Zhou, S. Dynamic gesture recognition based on 2D convolutional neural network and feature fusion. *Scientific Reports* **12**, 1-15 (2022).

46 Tekin, B., Bogo, F. & Pollefeys, M. in *Proceedings of the IEEE/CVF conference on computer vision and pattern recognition.* 4511-4520.

47 Ge, L. *et al.* in *Proceedings of the IEEE/CVF Conference on Computer Vision and Pattern Recognition.* 10833-10842.

48 Malik, J., Elhayek, A. & Stricker, D. in *International Conference on Virtual Reality and Augmented Reality.* 3-17 (Springer).

49 Glauser, O., Wu, S., Panozzo, D., Hilliges, O. & Sorkine-Hornung, O. Interactive hand pose estimation using a stretch-sensing soft glove. *ACM Transactions on Graphics (ToG)* **38**, 1-15 (2019).

50 Shen, Z. *et al.* A soft stretchable bending sensor and data glove applications. *Robotics and Biomimetics* **3**, 1-8 (2016).

51 Mummadi, C. K. *et al.* in *Informatics.* 28 (MDPI).

52 Liu, Y., Zhang, S. & Gowda, M. in *Proceedings of the Web Conference 2021.* 1471-1482.

53 Hong, Y., Sui, L., Zhang, M. & Shi, G. Theoretical analysis and experimental study of the effect of the neutral plane of a composite piezoelectric cantilever. *Energy conversion and management* **171**, 1020-1029 (2018).

54 McIntosh, J., Marzo, A., Fraser, M. & Phillips, C. in *Proceedings of the 2017 CHI Conference on Human Factors in Computing Systems.* 1923-1934.

55 Xia, W., Zhou, Y., Yang, X., He, K. & Liu, H. Toward portable hybrid surface electromyography/a-mode ultrasound sensing for human–machine interface. *IEEE Sensors Journal* **19**, 5219-5228 (2019).

56 Zhou, Z. *et al.* Sign-to-speech translation using machine-learning-assisted stretchable sensor arrays. *Nature Electronics* **3**, 571-578 (2020).

57 Wang, M. *et al.* Gesture recognition using a bioinspired learning architecture that integrates visual data with somatosensory data from stretchable sensors. *Nature Electronics* **3**, 563-570 (2020).

58 Tang, L., Shang, J. & Jiang, X. Multilayered electronic transfer tattoo that can enable the crease amplification effect. *Science Advances* **7**, eabe3778 (2021).

59 Wu, Y., Zheng, B. & Zhao, Y. in *2018 Chinese Automation Congress (CAC).* 2446-2450 (IEEE).

60 Ozyagcilar, T. Implementing a tilt-compensated eCompass using accelerometer and magnetometer sensors. *Freescale semiconductor, AN* **4248** (2012).

61 David Pirogovsky, A. N., Alec Newport. *Constellation Glasses*, https://people.ece.cornell.edu/land/courses/ece4760/FinalProjects/f2018/dap263_acn55_pdd35/dap263_acn55_pdd35/index.html

62 Gabriel, D. A. Teaching Essential EMG Theory to Kinesiologists and Physical Therapists Using Analogies Visual Descriptions, and Qualitative Analysis of Biophysical Concepts. *Sensors* **22**, 6555 (2022).

63 Konrad, P. The abc of emg. *A practical introduction to kinesiological electromyography* **1**, 30-35 (2005).

64 Cohen, E. *et al.* Excursion-volume relation of the right hemidiaphragm measured by ultrasonography and respiratory airflow measurements. *Thorax* **49**, 885-889 (1994).

65 Guarracino, F. *et al.* Lung, heart, vascular, and diaphragm ultrasound examination of COVID-19 patients: a comprehensive approach. *Journal of Cardiothoracic and Vascular Anesthesia* **35**, 1866-1874 (2021).

66 Nazmi, N. *et al.* Assessment on stationarity of EMG signals with different windows size during isotonic contractions. *Applied Sciences* **7**, 1050 (2017).

67 Pallotti, A., Orengo, G. & Saggio, G. Measurements comparison of finger joint angles in hand postures between an sEMG armband and a sensory glove. *Biocybernetics and Biomedical Engineering* **41**, 605-616 (2021).

68 Ortenzi, V., Tarantino, S., Castellini, C. & Cipriani, C. in *2015 IEEE International Conference on Rehabilitation Robotics (ICORR).* 1-6 (IEEE).

69 Bi, L. & Guan, C. A review on EMG-based motor intention prediction of continuous human upper limb motion for human-robot collaboration. *Biomedical Signal Processing and Control* **51**, 113-127 (2019).

70 Hu, H. *et al.* Stretchable ultrasonic arrays for the three-dimensional mapping of the modulus of deep tissue. *Nature Biomedical Engineering* **7**, 1321-1334 (2023).

71 Lin, M. *et al.* A fully integrated wearable ultrasound system to monitor deep tissues in moving subjects. *Nature Biotechnology* **42**, 448-457 (2024).

72 Akhlaghi, N. *et al.* Real-time classification of hand motions using ultrasound imaging of forearm muscles. *IEEE Transactions on Biomedical Engineering* **63**, 1687-1698 (2015).

73 Yang, X., Zhou, D., Zhou, Y., Huang, Y. & Liu, H. Towards zero re-training for long-term hand gesture recognition via ultrasound sensing. *IEEE Journal of Biomedical and Health Informatics* **23**, 1639-1646 (2018).

74 He, J., Luo, H., Jia, J., Yeow, J. T. & Jiang, N. Wrist and finger gesture recognition with single-element ultrasound signals: A comparison with single-channel surface electromyogram. *IEEE Transactions on Biomedical Engineering* **66**, 1277-1284 (2018).

75 Fernandes, A., Ono, Y. & Ukwatta, E. in *2020 IEEE International Conference on Flexible and Printable Sensors and Systems (FLEPS).* 1-4 (IEEE).

76 Yang, X., Yan, J., Fang, Y., Zhou, D. & Liu, H. Simultaneous prediction of wrist/hand motion via wearable ultrasound sensing. *IEEE Transactions on Neural Systems and Rehabilitation Engineering* **28**, 970-977 (2020).

77 Iravantchi, Y., Zhang, Y., Bernitsas, E., Goel, M. & Harrison, C. in *Proceedings of the 2019 CHI Conference on Human Factors in Computing Systems.* 1-13.

78 Xue, X. *et al.* Development of a wearable ultrasound transducer for sensing muscle activities in assistive robotics applications. *Biosensors* **13**, 134 (2023).

79 Zhang, X., Huang, H. & Yang, Q. in *2013 35th Annual International Conference of the IEEE Engineering in Medicine and Biology Society (EMBC).* 5926-5929 (IEEE).

80 Purushothaman, G. & Ray, K. EMG based man–machine interaction—A pattern recognition research platform. *Robotics and Autonomous Systems* **62**, 864-870 (2014).

81 Ju, Z. & Liu, H. Human hand motion analysis with multisensory information. *IEEE/AsMe Transactions on Mechatronics* **19**, 456-466 (2013).

82 Al-Timemy, A. H., Bugmann, G., Escudero, J. & Outram, N. Classification of finger movements for the dexterous hand prosthesis control with surface electromyography. *IEEE Journal of Biomedical and Health informatics* **17**, 608-618 (2013).

83 Peng, L. *et al.* in *2015 International Conference on Advanced Mechatronic Systems (ICAMechS).* 365-369 (IEEE).

84 Boschmann, A., Platzner, M., Robrecht, M., Hahn, M. & Winkler, M. (Myoelectric Symposium).

85 Stango, A., Negro, F. & Farina, D. Spatial correlation of high density EMG signals provides features robust to electrode number and shift in pattern recognition for myocontrol. *IEEE Transactions on Neural Systems and Rehabilitation Engineering* **23**, 189-198 (2014).

86 Liu, J. & Zhou, P. A novel myoelectric pattern recognition strategy for hand function restoration after incomplete cervical spinal cord injury. *IEEE Transactions on Neural Systems and Rehabilitation Engineering* **21**, 96-103 (2012).

87 Paleari, M., Di Girolamo, M., Celadon, N., Favetto, A. & Ariano, P. in *2015 37th Annual International Conference of the IEEE Engineering in Medicine and Biology Society (EMBC).* 6086-6089 (IEEE).

88 Pan, L., Zhang, D., Liu, J., Sheng, X. & Zhu, X. Continuous estimation of finger joint angles under different static wrist motions from surface EMG signals. *Biomedical Signal Processing and Control* **14**, 265-271 (2014).

89 Stapornchaisit, S., Kim, Y., Takagi, A., Yoshimura, N. & Koike, Y. Finger angle estimation from array EMG system using linear regression model with independent component analysis. *Frontiers in Neurorobotics* **13**, 75 (2019).